Micron-resolution fiber mapping in histology independent of sample preparation

Marios Georgiadis[1], Franca auf der Heiden[2], Hamed Abbasi[3,4], Loes Ettema[3], Jeffrey Nirschl[5], Hossein Moein Taghavi[1], Moe Wakatsuki[1], Andy Liu[1], William Hai Dang Ho[1], Mackenzie Carlson[1,6], Michail Doukas[7], Sjors A. Koppes[7], Stijn Keereweer[4], Raymond A. Sobel[5], Kawin Setsompop[1], Congyu Liao[1], Katrin Amunts[2,8], Markus Axer[2,9], Michael Zeineh[1], Miriam Menzel[3,2]

[1]Department of Radiology, Stanford University, Stanford, CA 94305, USA.
[2]Institute of Neuroscience and Medicine (INM-1), Forschungszentrum Jülich GmbH, Jülich, Germany.
[3]Department of Imaging Physics, Faculty of Applied Sciences, Delft University of Technology, Delft, the Netherlands.
[4]Department of Otorhinolaryngology and Head and Neck Surgery, Erasmus MC, University Medical Center Rotterdam, Rotterdam, the Netherlands.
[5]Department of Pathology, Stanford University, Stanford, CA 94305, USA.
[6]Department of Neurology and Neurological Sciences, Stanford University, Stanford, CA 94305, USA.
[7]Department of Pathology, Erasmus MC, University Medical Center Rotterdam, Rotterdam, the Netherlands.
[8]C. and O. Vogt Institute for Brain Research, University Hospital Düsseldorf, Medical Faculty, University Düsseldorf, Germany.
[9]Department of Physics, School of Mathematics and Natural Sciences, University of Wuppertal, Wuppertal, Germany.

Correspondence and requests should be addressed to Marios Georgiadis (email: mariosg@stanford.edu) and Miriam Menzel (email: m.menzel@tudelft.nl).

Abstract

Mapping the brain's fiber network is crucial for understanding its function and malfunction, but resolving nerve trajectories over large fields of view is challenging. Electron microscopy only studies small brain volumes, diffusion magnetic resonance imaging (dMRI) has limited spatial resolution, and polarization microscopy provides unidirectional orientations in birefringence-preserving tissues. Scattered light imaging (SLI) has previously enabled micron-resolution mapping of multi-directional fibers in unstained brain cryo-sections. Here, we show that using a highly sensitive setup, computational SLI (ComSLI) can map fiber networks in histology independent of sample preparation, also in formalin-fixed paraffin-embedded (FFPE) tissues including whole human brain sections. We showcase this method in new and archived, animal and human brain sections, for different stains and steps of sample preparation (in paraffin, deparaffinized, stained) and for unstained fresh-frozen samples. Employing novel analyses, we convert microscopic orientations to microstructure-informed fiber orientation distributions (μFODs). Adapting MR tractography tools, we trace axonal trajectories via orientation distribution functions and microstructure-derived tractograms revealing white and gray matter connectivity. These allow us to identify altered microstructure in multiple sclerosis and leukoencephalopathy, reveal deficient tracts in hippocampal sclerosis and Alzheimer's disease, and show key advantages over dMRI, polarization microscopy, and structure tensor analysis. Finally, we map fibers in non-brain tissues, including muscle, bone, and blood vessels, unveiling the tissue's function. Our cost-effective, versatile approach enables micron-resolution studies of intricate fiber networks across tissues, species, diseases, and sample preparations, offering new dimensions to neuroscientific and biomedical research.

Introduction

The brain contains billions of nerve fibers that form a highly complex and densely interwoven network. Detailed mapping of the neuronal trajectories is a major goal of neuroscience[1,2]. However, disentangling the fiber architecture with micrometer resolution and over large fields of view remains prohibitive: diffusion magnetic resonance imaging (dMRI) maps nerve fiber pathways in whole human brains with millimeter resolution, and even with long scan times in post-mortem brains it still probes hundreds of variably-oriented axons per voxel[3,4]. Electron microscopy resolves nerve cells at nanometer resolution[5,6], but tracking the fiber pathways is limited to small tissue volumes[7,8]. Small-angle X-ray scattering (SAXS) can directly probe multi-directional nerve fiber pathways[9,10], yet cannot provide whole-brain micrometer resolution and requires expensive equipment such as synchrotrons. Various light microscopy techniques visualize nerve fibers at high resolution and over larger fields of view, using staining[11,12], fluorescence[13], or other contrast mechanisms. However, they rely on structure tensor analysis to derive fiber orientations[14,15], which decreases effective resolution and is limited in resolving crossing or densely packed nerve fibers. Polarization-based techniques directly visualize fiber orientations exploiting their birefringence[16,17], with 3D-polarized light imaging (3D-PLI) being the current gold standard for analyzing nerve fiber architecture in whole human brain sections[18–20]. In spite of this, 3D-PLI analysis yields only unidirectional fiber orientations per pixel, and tissue preparation needs to preserve birefringence, e.g., by avoiding dehydration and lipid removal. Recently, scattered light imaging (SLI) has emerged as a method to reveal multi-directional, densely interwoven nerve fiber networks in unstained brain cryo-sections with micrometer resolution, using a stationary LED matrix display and a camera to probe the anisotropic scattering of the sample[21–23].

At the same time, the most common tissue preparation method in histology is paraffin embedding and microtome sectioning followed by histological staining[24]. These formalin-fixed paraffin-embedded (FFPE) sections, which are abundantly available in hospital pathology archives as well as in research and clinical laboratories, cannot be analyzed by polarization-based techniques because the birefringence is significantly reduced during tissue preparation. One prominent example is the *BigBrain* atlas[11], containing thousands of FFPE sections of a whole human brain. Nissl-based structure tensor analysis (Nissl-ST) can be used to track white matter fibers in FFPE brain sections by analyzing the arrangement of glial cells to derive nerve fiber directions[25]. However, Nissl-ST can only be applied to sections with Nissl staining. Furthermore, it has an effective resolution of tens of micrometers, and similar to polarization microscopy, it does not resolve multi-directional, crossing fibers per pixel which are abundant in the brain.

Here, we show that computational scattered light imaging (ComSLI) – a fast and cost-effective optical microscopy method that uses a directed rotating LED light and a high-resolution camera for improved signal-to-noise ratio – can reveal microscopic, multi-directional fiber orientations of virtually any new and archived tissue section, including FFPE and fresh-frozen sections. Using ComSLI, we recover fiber orientation maps from animal and human brain tissues prepared

with different protocols, stains, thicknesses, and storage periods – including whole-brain sections from the *BigBrain* atlas[11]. We leverage the micron-resolution fiber orientation information to obtain ground-truth, microstructure-derived fiber orientation distributions (μFODs) over a range of resolutions, and use those to perform fiber tractography, resulting in microstructure-informed tractograms reflecting axonal trajectories. We show that our technique reconstructs fiber microarchitecture in healthy and diseased tissue – discerning myelin from axonal loss, revealing microstructural alterations in multiple sclerosis and leukoencephalopathy, and identifying degeneration of the perforant pathway in sclerotic and Alzheimer's Disease hippocampus tissue. By comparing ComSLI to dMRI, 3D-PLI, and Nissl-ST, we demonstrate its key advantages in revealing highly detailed and interwoven fiber networks, including micron-resolution nerve fiber architecture in whole-brain FFPE sections. Finally, we show that our technique can also be applied to reveal directed structures in non-brain tissues, like muscle and collagen fibers.

Our approach enables retrospective investigations of histology slides, combining information from any stain with fiber orientations. Furthermore, it can help reveal new micro-organization patterns as well as relationships between the microstructure and the underlying biology in healthy and diseased, animal and human tissues.

Results

Revealing microscopic fiber architecture in whole human brain sections

Spatially oriented structures such as nerve fibers scatter light predominantly perpendicular to their main axis[26], yielding characteristic light intensity profiles, $I(\varphi)$, where the mid-position of a peak pair indicates the fiber orientation (Fig. 1A). ComSLI reverses the light path, which is physically equivalent, to determine the orientations of fibers contained in each micrometer-sized image pixel. A rotating LED light source illuminates the tissue section at ~45° elevation, and a high-resolution camera with small-acceptance-angle lens captures sample images at multiple light source rotation angles φ (Fig. 1B). This yields an image series in which each pixel contains a light intensity profile across different illumination angles, $I(\varphi)$, according to the orientation of its contained fibers (Supplementary Movie 1). Analyzing the peak positions in each pixel's intensity profile yields fiber orientations, with example intensity profiles for single and two crossing fiber populations shown in Fig. 1G, with the signal also visualized as polar plot (see insets).

First, we tested if ComSLI can retrieve fiber orientations with micrometer resolution from extended field-of-view sections, such as entire FFPE human brain sections from *Jülich BigBrain*[11] (Fig. 1C, inset at top right). Orientation information was recovered from single and crossing fiber bundles in each pixel, in white and gray matter (Fig. 1C). Microscopic details become apparent: Corpus callosum (cc) fibers decussate between the two hemispheres with small angular variations (Fig. 1D, small arrows), while fornix (f) fibers course superomedially, and multiple fibers cross in dense corona radiata (cr) white matter (Fig. 1E). U-fibers connect the precentral to neighboring gyri (Fig. 1F), with subjacent deeper fibers crossing the main tracts (small arrows).

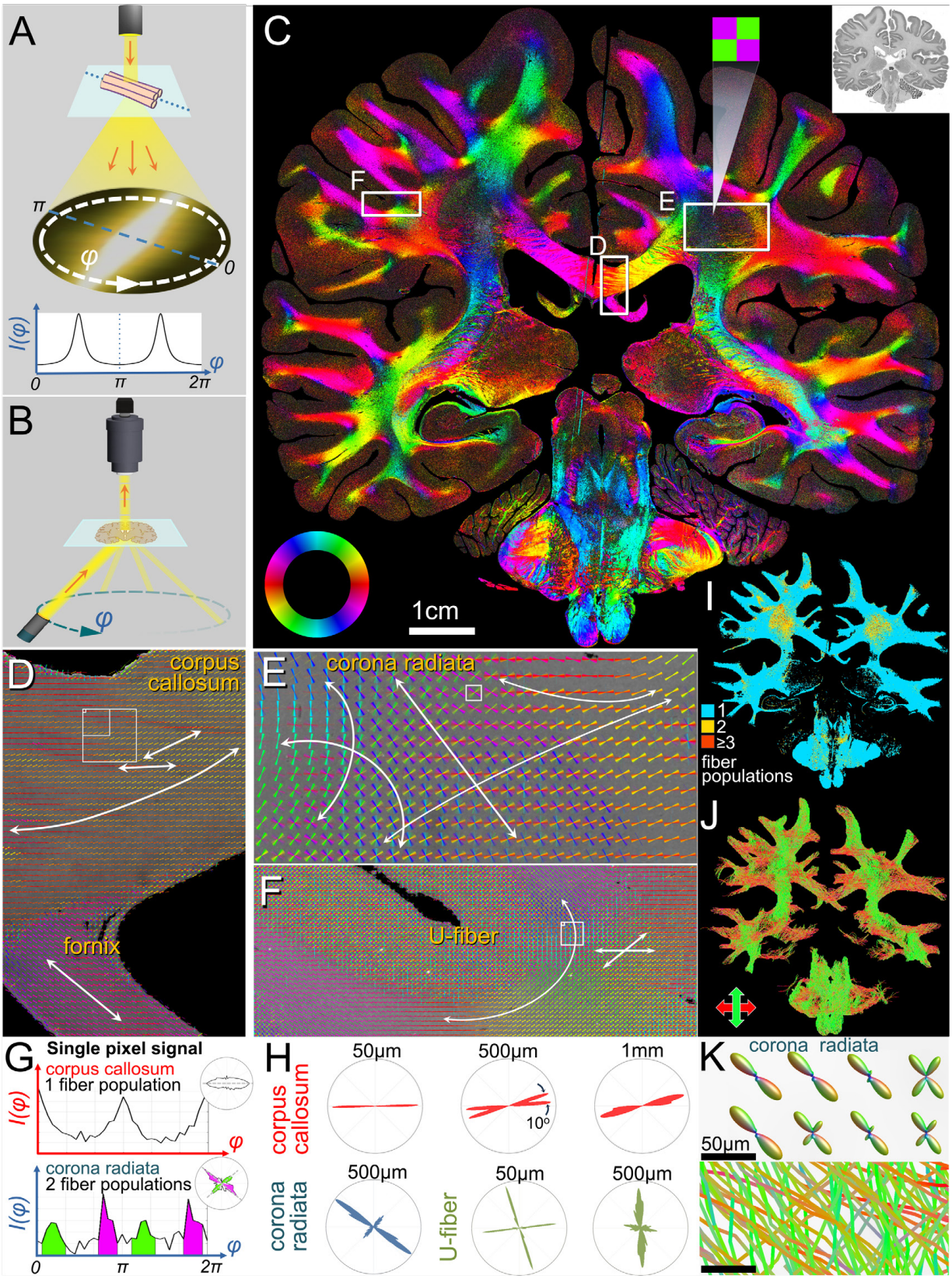

Fig. 1 | Retrieving microscopic fiber orientations in a whole human brain section. (**A**) A light beam impinging on a fiber bundle scatters predominantly perpendicular to the fibers, resulting in paired peaks in the azimuthal intensity profile, $I(\varphi)$, whose midline indicates the fiber orientation. (**B**) Schematic of ComSLI measurement setup, reversing

the light path to measure each pixel's azimuthal intensity profile. The tissue section is illuminated at ~45° elevation by a rotating light source while a camera captures a high-resolution image of the section at each azimuthal rotation angle φ. (**C**) Fiber orientation map (7µm/pixel) of the second *BigBrain* dataset, section no. 3452, FFPE, silver-stained. The inset shows the corresponding brightfield image, 1µm/pixel. The fiber orientations are shown as multi-colored pixels according to the color wheel in the bottom left; multiple colors per pixel indicate multiple fiber orientations, such as the zoomed-in green-purple corona radiata pixel. (**D-F**) Fiber orientations for boxes marked in C. Orientations are encoded both by the line direction and its color. (**D**) Corpus callosum (cc) and fornix (f). (**E**) Right corona radiata (cr). (**F**) U-fiber. (For better visualization, the orientation-depicting lines of sets of 15x15 pixels (D,F) and 75x75 pixels (E) are overlaid). (**G**) Azimuthal intensity signals from pixels with single and crossing fiber populations, at the smallest squares in D and E respectively, also shown as polar plots (top right insets). The polar plots were rotated by 90° to better visualize fiber orientations. (**H**) Microstructure-derived fiber orientation distributions (µFODs), showing the fiber directions in a polar histogram for all image pixels in the squares indicated in D-F. (**I**) Map of the number of fiber populations in each 7µm pixel of the white matter. (**J**) Tractogram of the entire brain, top-bottom fibers are shown in green, left-right fibers in red. (**K**) Corona radiata detail of microscopic orientation distribution functions (ODFs) for kernels of 7x7 pixels, and tracts crossing the same pixels (from the top left corner of the small square in E).

Being able to detect multiple fiber orientations per pixel at micrometer scale, we then sought to study their distribution across scales. Namely, this can help to better understand the fiber distribution in MRI voxels, which are hundreds of micrometers to millimeters in size and typically contain thousands of axons. Figure 1H shows the microstructure-derived fiber orientation distributions (µFODs) for the highlighted points in the corpus callosum, corona radiata, and U-fibers (squares in Figs. 1D-F) in the form of polar histograms, for a range of different scales. For instance, in the corpus callosum, a grid of 7x7 pixels (corresponding to ~50µm resolution) shows high horizontal alignment, whereas at 500µm (71x71 pixels), there are two fiber populations 10° apart, which would be misinterpreted by dMRI as single fiber population due to its ~40°-45° maximum sensitivity for discerning crossing fibers[27,28]. In contrast, at 1mm, the different fiber populations cannot be distinguished anymore.

Such multi-scale fiber distributions are rich in information. For instance, one can calculate how many brain pixels contain crossing fibers at the microscopic ComSLI resolution (Fig. 1I), and at multiple other resolutions common for MRI scanning (Supplementary Fig. 1). This reveals that only ~7% of pixels at 7µm resolution contain two or more crossing fibers, but this rises to 87% and 95% for 500µm and 1mm pixel resolution.

Finally, the fiber orientation distributions also enable tractography: Adapting tools employed in MR tractography, we generated orientation distribution functions (ODFs) uniquely informed by our micrometer-level fiber orientations (see Methods), and used these to produce whole-brain white matter tractograms (Fig. 1J), with microscopic ODFs and tract lines for a corona radiata region shown in Fig. 1K. The ODF and tractography analysis enable detailed study of microstructure-based connectivity in white and gray matter of the whole brain (Supplementary Fig. 2A), and in specific anatomic regions, with some examples shown in Supplementary Fig. 2B-E, such as white and gray matter of the precentral gyrus, a pre/post-central gyrus U-fiber, the corona radiata, and the corpus callosum. The data and code to generate the whole brain tractogram are publicly available, see Data and Code Availability sections.

Such investigations at whole-brain level unveil microscopic fiber orientations, enabling detailed investigation of anatomy, correlations with cellular information, and pathology.

ComSLI works across stains, preparation protocols, and species

Next, we tested whether ComSLI can retrieve information from histological sections across stains, sample preparations, and species, since the orientation of scattered light is affected solely by the orientation of scattering fibers.

We scanned consecutive FFPE sections of a human hippocampus with various stains, colors, intensities, antibody concentrations, and counter-stains (see Methods). Figure 2 and Supplementary Fig. 3 show the brightfield images (A), fiber orientation maps (B), and zoomed-in views of the cornu ammonis and multiple fiber tracts (C). Despite the different staining protocols, targets, intensities, and counter-stains, the retrieved fiber orientations are almost identical across hippocampal sections, with small anatomical differences between sections (see difference maps and corresponding histograms in Fig. 2D).

We also investigated a celloidin-embedded section, myelin-stained ~120 years ago, from the brain collection of the Cécile and Oskar Vogt Institute for Brain Research (Fig. 2E-F). Despite the section age and the low light transmission in parts of the section (Fig. 2E), detailed nerve fiber orientations were retrieved (Fig. 2F), e.g., in the corpus callosum and the Muratoff bundle (subcallosal fasciculus) running subependymal to the caudate nucleus surface[29] (arrowhead).

This led us to ask (i) if we can also retrieve orientations from sections at different steps of sample preparation, and (ii) if the sample processing affects the method's sensitivity. We scanned two sections in 3 different steps: 1) in paraffin after sectioning, 2) after deparaffinization, and 3) after staining (Supplementary Fig. 4). Excitingly, fiber orientations could be visualized from sections still in paraffin (Supplementary Fig. 4A-B), as well as from unstained sections (Supplementary Fig. 4C-D), showing similar results as the stained sections (Supplementary Fig. 4E-F). The derivation and concordance of white and gray matter orientations across sample preparation stages highlight the wide range of histology sections that can be analyzed with ComSLI.

While FFPE sections are gold standard in histological tissue analysis, fresh-frozen samples are also common, allowing fast diagnosis during surgery or better preservation of molecular targets. Here, we show that ComSLI can retrieve fiber orientations in human brain tissues fresh-frozen after autopsy without fixation or staining, such as human visual cortex and hippocampal sections (Supplementary Fig. 5).

To confirm that the technique works across species, we measured multiple animal brain FFPE sections with different stains, including from mouse (Fig. 2G-J) and pig (Fig. 2K-N). Tracts were retrieved with micrometer resolution, such as the intricate mouse cerebellar connectivity (Fig. 2J) and multiple crossing and U-fibers in the pig corona radiata (Fig. 2N).

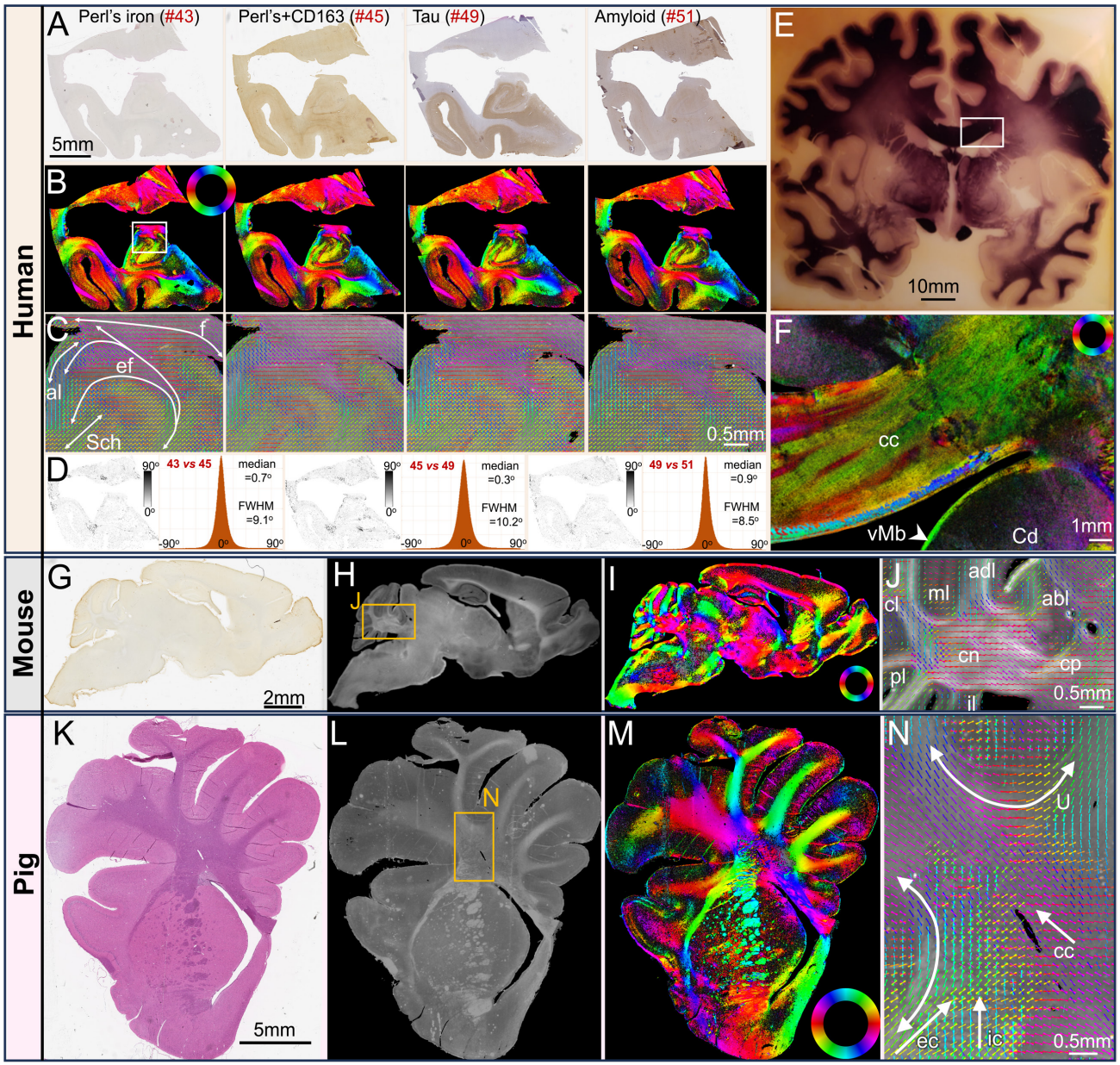

Fig. 2 | ComSLI detects fiber orientations independent of tissue preparation and species. (**A-C**) **Human Hippocampi**, FFPE sections with different stains. (**A**) Brightfield microscopy images, 0.5µm/pixel. (**B**) ComSLI fiber orientation maps, 7µm/pixel, orientations encoded by color wheel. (**C**) Zoomed-in fiber orientation vector maps (white box in (B)), including parts of cornu ammonis and multiple tracts: fornix (f), endfolial pathway (ef), alveus (al), Schaffer collaterals (Sch). Vectors of 15x15 pixels are overlaid. (**D**) Orientation difference for each pair of consecutive sections, as map (left) and histogram (right), with medial value and full-width-half-maximum (FWHM) reported. (**E-F**) **Myelin-stained human brain section** (~120-year-old). (**E**) Section photograph. (**F**) ComSLI color-coded fiber orientation map (3µm/pixel) of marked region in (E), cc: corpus callosum, Cd: Caudate nucleus, MB: Muratoff bundle (arrowhead). (**G-J**) **Sagittal mouse brain section**, FFPE, microglia-stained. (**G**) Brightfield image, 0.5µm/pixel. (**H**) ComSLI average scattering signal, 4.25µm/pixel. (**I**) Fiber orientation map. (**J**) Zoom-in of box in (H) (cerebellar area), including cerebellar peduncle (cp), cerebellar nuclei (cn), lobes (inferior-il, posterior-pl, central-cl, anterodorsal-adl, anterobasal-abl), and gray matter including oriented molecular layer (ml) fibers. Vectors overlaid for 15x15 pixels. (**K-N**) **Pig hemisphere-brain section**, FFPE, H&E-stained. (**K**) Brightfield image, 0.5µm/pixel. (**L**) ComSLI average scattering signal, 9µm/pixel. (**M**) Fiber orientation map. (**N**) Fiber orientations from box in (L), overlaid for 15x15 pixels, including U-fiber tracts (curved arrows) and multiple crossing fibers (straight arrows); external capsule (ec), internal capsule (ic), corpus callosum (cc).

Detecting disturbed microarchitecture in pathologic tissues

To test if ComSLI can unveil disturbed microscopic fiber orientations and provide unique information in pathologic human tissue, we studied human brain samples with neuropathology.

First, we investigated a brain of a subject with multiple sclerosis – a neurological autoimmune disease damaging the insulating myelin sheaths of nerve fibers and impairing signal transmission. We imaged a section with focal demyelination (Fig. 3A, red-annotated lesions). To fully characterize the lesion pathologically, we performed additional myelin (Luxol fast blue -LFB) and neurofilament stains in consecutive sections (Fig. 3J,L, and Supplementary Figs. 6,7). Three lesion areas are noted based on histology (arrows 1-3 in Fig. 3A,B,J): lesion area 1 has demyelination and lower neuropil density, while lesion areas 2 and 3 show demyelination only. Higher magnification of characteristic regions in lesion area 1 (demyelination and neuropil loss), lesion area 2 (demyelination), and normal white matter (region 4) are shown in Fig. 3L, for neurofilament staining.

The light scattering signal (Fig. 3B) was not affected by myelin loss (lesion areas 2 and 3), but only by lower neuropil density (lesion area 1). Interestingly, the axonal orientations could be retrieved in all regions, including extensive demyelination and neuropil loss (Fig. 3C). In regions of transition between normal white matter (nwm) and demyelinated white matter (dwm) at the edge of lesion 3 (Fig. 3D-F), the ComSLI signal intensity is preserved, and the fibers seem to continue their course despite demyelination. This highlights the robustness of the method, which retrieves axonal orientations independent of myelin, also for gray matter (gm) axons (Fig. 3D-E). In addition, ComSLI detects changes in tissue density: the neuropil loss in lesion 1 leads to lower ComSLI signal (Fig. 3B) and fiber organization (Fig. 3G,H), which is detected by ComSLI based on the remaining axons. Signal preservation despite demyelination and sensitivity to neuropil loss is shown in Fig. 3K, where the three lesions (areas 1-3) have a lower myelin histology signal than the nwm regions (areas 4-5), but only lesion 1 has lower average scattering signal.

Next, we studied an H&E section from a necrotizing leukoencephalopathy brain (Fig. 3M) which is characterized by white matter necrosis with loss of neurons and myelin, confirmed with LFB and neurofilament stains on consecutive sections (Fig. 3R,U), showing patchy axon loss and spongiosis as well as axonal spheroids and dystrophic axons (Supplementary Fig. 6I,J). The three pathology-confirmed lesion areas (indicated by arrows and red-contoured in Fig. 3M) depict a low myelin histology signal, but lesion area 3 shows a higher average scattering signal than lesions 1-2 (Fig. 3W). Upon close pathology review, lesion area 3 has less necrotizing tissue (Fig. 3S), not initially noted by an expert pathologist but later observed due to the scattering signal preservation, confirming the method's sensitivity to tissue loss. The lesions are located within the corona radiata (cr) where multiple nerve fiber crossings occur; the fiber orientation map (Fig. 3O) reveals the intricate fiber organization in this region, with grayish-appearing color showing crossing fibers of multiple orientations. A closer look (Fig. 3Q,T) shows the multiple crossings

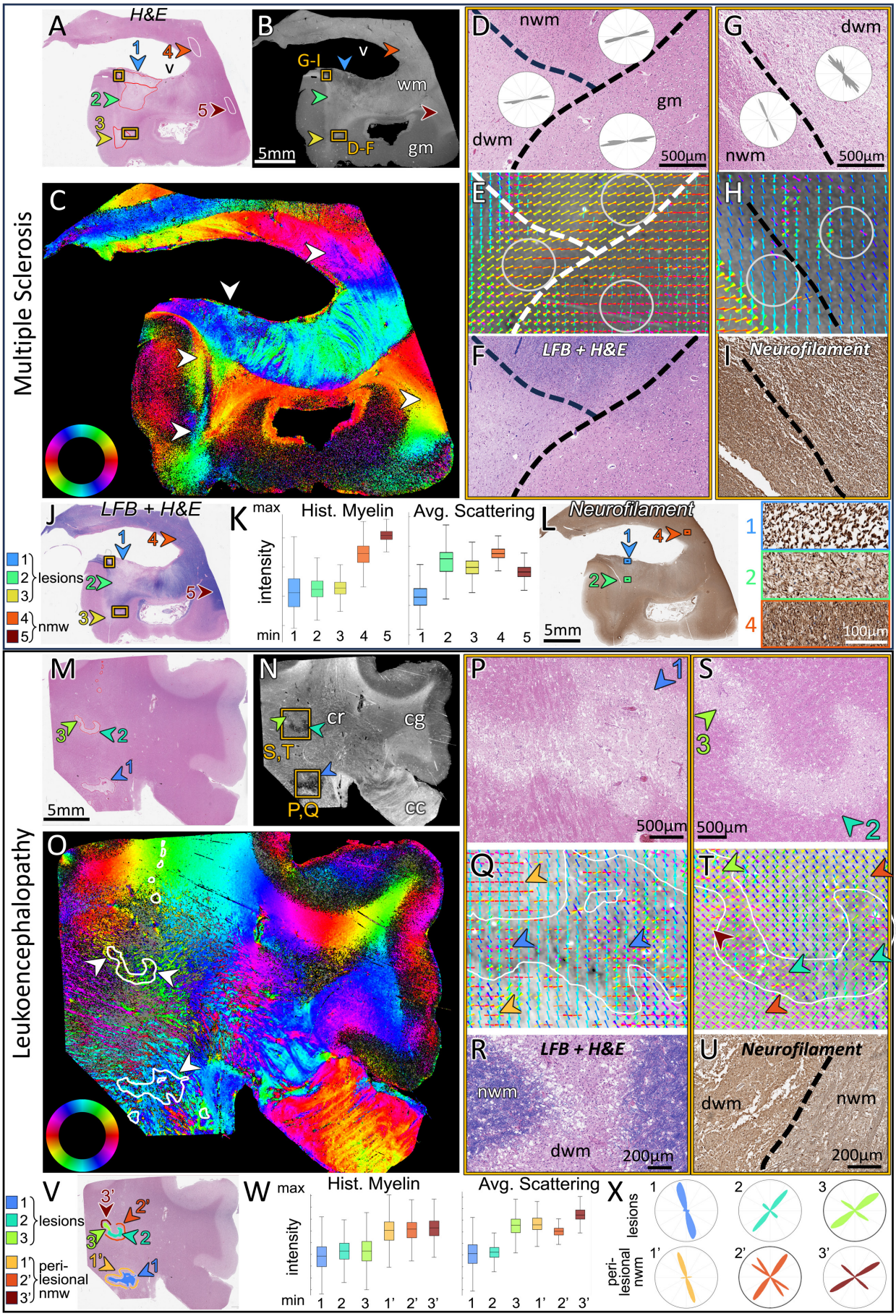
Multiple Sclerosis
A
H&E
B
G-I
v
wm
gm
D-F
5mm
C
D
nwm
gm
dwm
500µm
G
dwm
nwm
500µm
E
H
F
LFB + H&E
I
Neurofilament
J
LFB + H&E
1
2
3
lesions
4
5
nmw
K
max
Hist. Myelin
Avg. Scattering
intensity
min
1 2 3 4 5
1 2 3 4 5
L
Neurofilament
5mm
100µm
Leukoencephalopathy
M
5mm
N
cr
cg
S,T
P,Q
cc
O
P
500µm
S
500µm
Q
T
R
LFB + H&E
nwm
dwm
200µm
U
Neurofilament
dwm
nwm
200µm
V
1
2
3
lesions
1'
2'
3'
peri-lesional nmw
W
max
Hist. Myelin
Avg. Scattering
intensity
min
1 2 3 1' 2' 3'
1 2 3 1' 2' 3'
X
lesions
peri-lesional nwm

Fig. 3 | Human brain pathology measured with ComSLI (FFPE sections, H&E-/LFB-/neurofilament-stained). Brightfield microscopy: 0.5µm/pixel, ComSLI: 9µm/pixel. (**A-L**) **Multiple sclerosis brain**. (**A**) Brightfield H&E image with lesion areas 1-3 (red contours) and normal white matter areas 4-5 (white contours). (**B**) Average scattering signal (v: ventricle, gm: gray matter, wm: white matter). (**C**) Fiber orientation map. (**D**) Zoom-in of H&E-stained lesion 3 (lower box in A-B), including normal white matter (nwm), demyelinated white matter (dwm), and gray matter (gm), with fiber distributions from underlying areas, also circled in E. (**E**) Corresponding fiber orientations. 15x15 pixel orientations are overlaid for visual clarity. (**F**) The same region in a consecutive LFB+H&E-stained section. (**G**) Zoom-in of H&E-stained lesion 1 (upper box in A-B), with fiber distributions from underlying areas, also circled in H. (**H**) Corresponding fiber orientations. (**I**) The same region in a consecutive neurofilament-stained section. (**J**) LFB+H&E-stained consecutive section, with lesion and nwm areas depicted. (**K**) Intensity of histology myelin stain and average ComSLI scattering for areas 1-5. (**L**) Neurofilament-stained consecutive section and zoom-ins of areas 1,2 and 4. (**M-X**) **Leukoencephalopathy brain**. (**M**) Brightfield H&E image with lesion areas 1-3 (red contours). (**N**) Average scattering signal. cc: corpus callosum, cg: cingulum, cr: corona radiata. (**O**) Fiber orientation map, lesions with white contour. (**P**) Zoom-in of H&E-stained lesion 1 (lower box in N). (**Q**) Corresponding fiber orientations, more aligned outside and less within the lesion (orange/blue arrows respectively). (**R**) Lesion zoom-in in LFB+H&E-stained consecutive section, showing dramatic myelin loss, axonal loss and spongiosis in lesion. (**S**) Zoom-in of H&E-stained lesions 2-3 (upper box in N). (**T**) Corresponding fiber orientations, with arrows highlighting aligned (perilesional and lesion 3) and heterogeneous (lesion 2) fiber orientations. (**U**) Lesion zoom-in in a neurofilament-stained consecutive section. (**V**) Lesions and nwm areas depicted. (**W**) Intensity of histology myelin stain and average ComSLI scattering for the three lesions (1-3) and their perilesional areas (1'-3'). (**X**) Fiber orientation distributions for the lesions and their perilesional nwm areas.

of the fibers both inside and surrounding the lesions, with fibers more heterogeneously distributed inside the lesions (example heterogeneous orientations are highlighted by the arrows), reflecting the disorganization associated with local tissue destruction. This is also quantitatively reflected in the µFODs shown in Fig. 3X, where the lesions show relatively preserved but more heterogeneous distributions than the corresponding perilesional normal white matter areas (exact areas are depicted in Fig. 3V). For instance, lesion area 1 seems to lose most of the horizontal fibers (orange arrows in Fig. 3Q), and lesion area 2 most of the two minor diagonal fiber populations (orange arrows in Fig. 3T).

We next focused on the hippocampus, a brain region key for memory and affected in neurodegeneration. We compared the hippocampal pathways in coronal sections of samples form three donors: one with epilepsy-associated hippocampal sclerosis, one with Alzheimer's Disease (AD), and an aged control, Supplementary Fig. 8. At a macroscopic level, the diminished volume of the sclerotic and AD hippocampi, Supplementary Fig. 8B',B", was accompanied by a strong degeneration of pathways, with very few remaining crossings across the sclerotic hippocampus and a greatly reduced number in the AD hippocampus compared to the control, Supplementary Fig. 8C,C',C". The perforant pathway (p), the principal source of entorhinal input to the hippocampus, overlying the medial subiculum, was almost completely degenerated in the sclerotic hippocampus and was very weak in the AD hippocampus, as shown with fiber orientations and resulting tractograms, Supplementary Fig. 8D'-F' and D"-F". On the other hand, the control hippocampus had multiple interwoven fibers across all subfields, Supplementary Fig. 8C, with an especially strong perforant pathway connecting the entorhinal cortex to CA1, CA3, and dentate gyrus, Supplementary Fig. 8D-F. Overall, ComSLI can reveal loss of distributed axonal networks associated with neurodegeneration.

Comparison to diffusion MRI, structure tensor analysis, and 3D-PLI

We compared ComSLI to previously developed methods that yield fiber orientations using different mechanisms and physical phenomena.

We first contrasted ComSLI to Nissl-based Structure Tensor (Nissl-ST)[25]. Nissl-ST uses 2D structure tensor analysis to retrieve fiber orientation information in white matter areas based on the anisotropic shape and alignment of Nissl-stained glial cells. We measured brain sections Nissl-stained with Cresyl violet (Fig. 4 and Supplementary Fig. 12), using the code and settings by Schurr & Mezer[25] to derive in-plane fiber orientations. Comparing Nissl-ST output for different kernel sizes, from 200x200µm to 50x50µm (Supplementary Fig. 9), the 100µm kernel showed the best balance between data quality and resolution, and was used in our analyses.

Contrasting ComSLI results on a whole human brain section (Fig. 4, left) to those obtained using Nissl-ST on the same section (Fig. 4, middle), the fiber orientations are in overall agreement between the two methods (Fig. 4A,A'). However, ComSLI achieves better visualization of small features in a label-free manner, such as fiber bundles in the putamen (Pu) and globus pallidus (GPe, GPi), the medial and lateral medullary laminae (mml, lml), and the external capsule (ec), Fig. 4B,B'. ComSLI also better resolves, e.g., the two fiber populations in the corpus callosum (Fig. 4C,C'). Moreover, ComSLI resolves multiple crossing fibers per 3µm pixel, for example in the corona radiata region (Fig. 4D), with Nissl-ST providing single fiber orientation per 100µm pixel (Fig. 4D'). This is exemplified by the fiber orientation distributions as shown in the insets, whereby Nissl-ST often misinterprets crossing fibers as single fibers at an intermediate angle.

Direct quantitative pixel-wise comparison between the orientation outputs of the two methods (Supplementary Figs. 10) reflects the aforementioned observations. The angle difference histogram is skewed towards 0° (Supplementary Fig. 10C,D), with small differences in the corpus callosum, but widespread angle differences in areas of crossing fibers such as the corona radiata (Supplementary Fig. 10B). This is also shown via the generated ComSLI ODFs in a corpus callosum and corona radiata area (Supplementary Fig. 10E and F), where the differences in pixel size (boxes), information content, and orientation accuracy become evident (the blue lines within the dashed boxes indicate the fiber orientation derived from Nissl-ST). This exemplifies the ability of ComSLI to capture much finer orientations, which also translates to microstructure-informed fiber tracts in both simple and complex crossing fiber areas (Supplementary Fig. 10G,H).

We also compared our results to fiber orientations from a high-resolution *in vivo* 18-hour diffusion MRI scan of a healthy volunteer's brain[30] (Fig. 4, right). ComSLI fiber orientations were compared to those from the MR plane best matching the measured brain sections (see Methods). The main nerve fiber orientation patterns of ComSLI and dMRI are in agreement (Fig. 4A,A''). However, ComSLI unveils distinct microscopic fiber orientation patterns, like the different fiber populations at low angles in the corpus callosum (Fig. 4C), which are bundled in a single fiber orientation in dMRI (Fig. 4C''), or the individual fiber bundles in the putamen and globus pallidus or the medullary laminae (Fig. 4B), not resolved by dMRI *in vivo* (Fig. 4B'') or *ex vivo*[31].

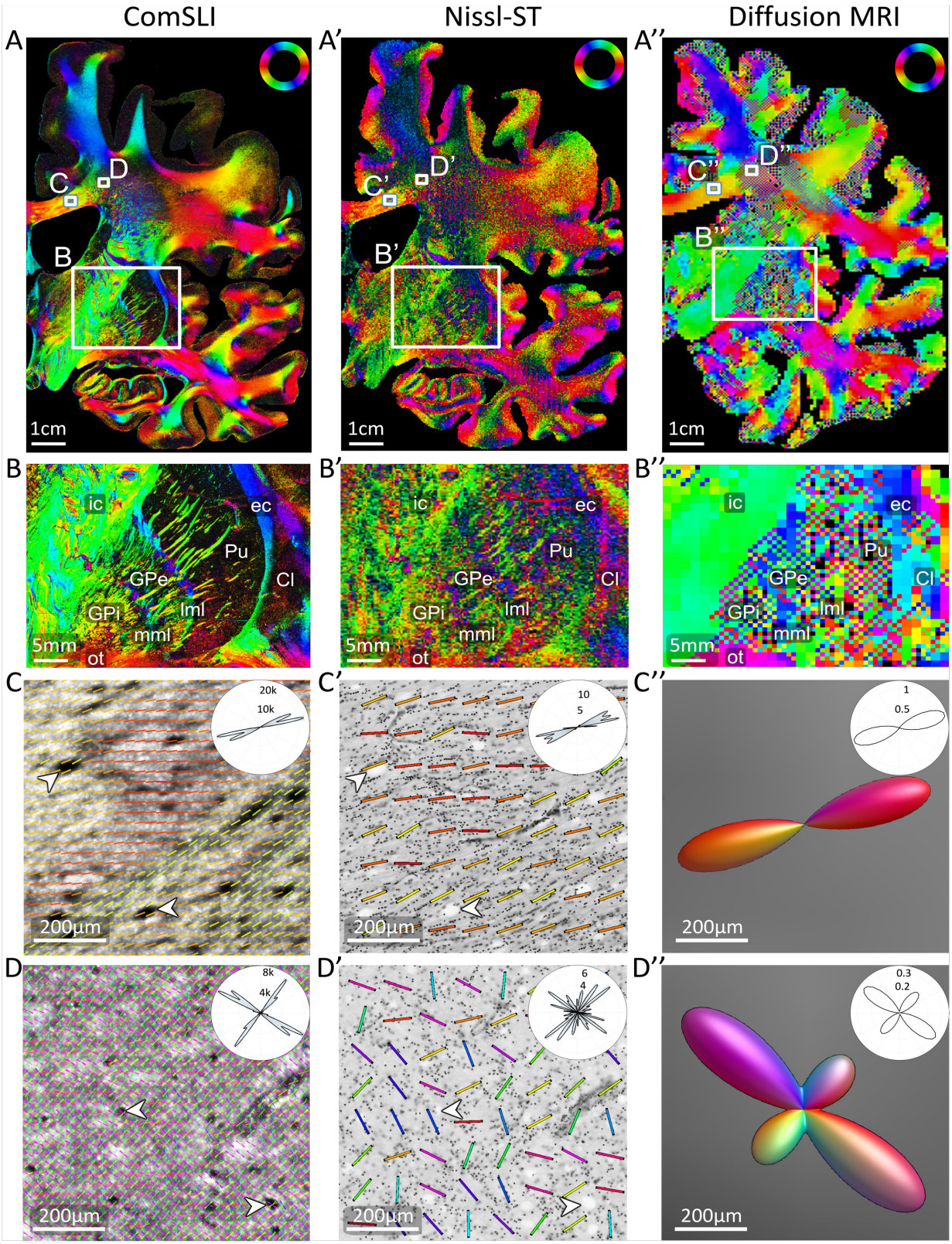

Fig. 4 | Comparison of ComSLI, Nissl-ST, and dMRI fiber orientations. ComSLI and Nissl-ST were performed on the same brain section (human coronal FFPE section, Nissl-stained with Cresyl violet, no. 3301) – the ComSLI measurement with 3µm pixel size, and Nissl-ST on the brightfield microscopy image with 1µm pixel size. Diffusion MRI was performed *in vivo* on a healthy volunteer with 0.76mm isotropic voxel size, and the orientation distribution

functions were evaluated at a plane similar to the evaluated brain section (see Methods). (**A**) Color-coded fiber orientations depicted for each image pixel. The orientations were computed with *SLIX*[34] for ComSLI and dMRI, and with the provided code for Nissl-ST[25] using 15µm blur radius and a kernel size of 100x100µm. (**B**) Enlarged views of the fiber orientation maps for the bottom rectangular area marked in (A), featuring individual fiber bundles in the globus pallidus and putamen; annotated are internal capsule (ic), external capsule (ec), optic tract (ot), globus pallidus external segment (GPe), globus pallidus internal segment (GPi), putamen (Pu), medial and lateral medullary laminae (mml, lml), and claustrum (Cl). (**C**) Enlarged views of the fiber orientations for the corpus callosum area corresponding to the size of a dMRI voxel (760µm), annotated by top left rectangle in (A). ComSLI fiber orientations were visualized as colored lines and overlaid on 10x10 pixels for better visualization; white arrows indicate the same microscopic features in ComSLI average scattering signal in C and histology in C'. Fiber orientation distributions for each modality are shown as insets in the top right. (**D**) Enlarged views of the fiber orientations for the corona radiata area corresponding to the size of a dMRI voxel (760µm), annotated by top right rectangle in (A). ComSLI fiber orientations were visualized as colored lines and overlaid on 10x10 pixels for better visualization; white arrows indicate the same microscopic features in ComSLI average scattering signal in D and histology in D'. Fiber orientation distributions for each modality are shown as insets in the top right. The dMRI orientation distribution functions in C'' and D'' were visualized with *MRtrix3*'s *mrview*[35].

A pixel-wise, quantitative comparison of ComSLI and Nissl-ST on a different brain section – the cell-body silver-stained *Jülich BigBrain* section from Fig. 1C – and comparison to in-vivo dMRI orientations from a corresponding plane yields similar conclusions (Supplementary Fig. 11).

Finally, 3D-Polarized Light Imaging (3D-PLI) provides micron-resolution fiber orientation maps of whole-brain sections[18–20]. Our tests on the studied whole-brain FFPE sections showed significantly reduced sensitivity (Supplementary Fig. 12, right), compared to the high-sensitivity high-resolution maps it provides in 3D-PLI sections. This is possibly because an important part of myelin lipids resolves during alcohol dehydration[32], and water removal also distorts myelin periodicity[33], resulting in loss of its birefringence.

Mapping fibers in histology beyond brain

Finally, we tested whether ComSLI can retrieve fiber orientations from non-brain human tissues, given the multiple fiber types present, often in close proximity. We performed measurements on FFPE sections from different tissue types (Fig. 5): human tongue muscle, colorectal tissue, lower jaw bone (mandible), and arterial wall.

In the tongue, ComSLI reveals layers of differently oriented structures (Fig. 5A-D), like outer epithelium (1), underlying stroma (2) with collagen fibers running mostly parallel to the surface, and inner muscular layer (3), which contains muscle fibers that enable tongue reshaping and multi-directional movement.

In the colorectal tissue (Fig. 5E-I), orientations of multiple fiber types are retrieved: epithelial lamina propria (1) is mostly oriented normally/radially to the surface, while basal membrane fibers are mostly oriented parallel to the surface (arrowheads in Fig. 5G); the mucosal and submucosal fibers (2) have a complex architecture with various orientations; circular muscle fibers of the muscularis mucosa (3) run from top to bottom (corresponding inset in Fig. 5G and lower arrowhead in Fig. 5H); longitudinal fibers of the muscularis propria (4) run mostly perpendicular to the circular muscle fibers (corresponding inset in Fig. 5G and upper arrowhead in Fig. 5H).

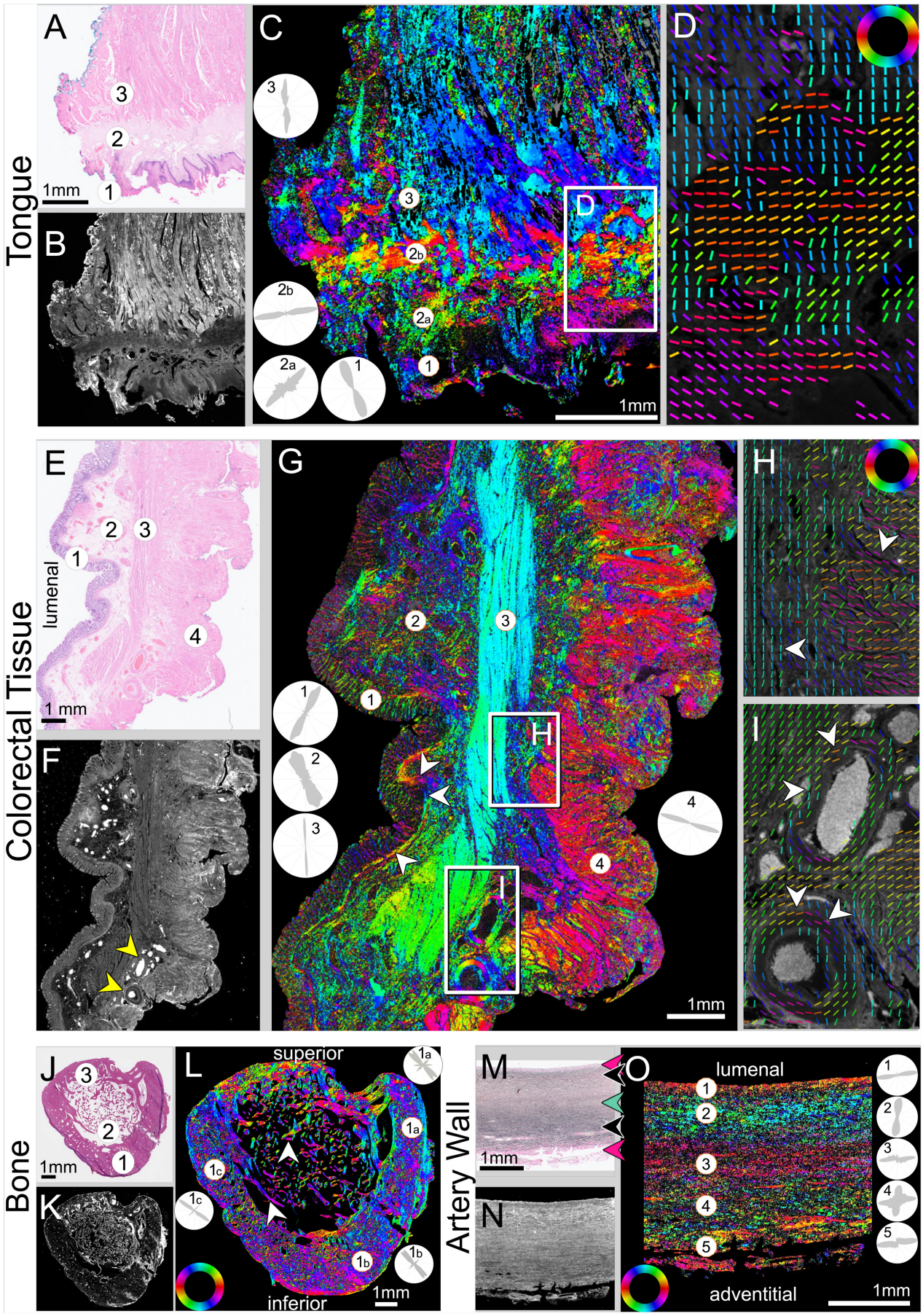
Tongue
A
B
C
D
1mm
Colorectal Tissue
E
F
G
H
I
lumenal
1 mm
1mm
Bone
J
K
L
superior
inferior
1mm
Artery Wall
M
N
O
lumenal
adventitial
1mm

Fig. 5 | Non-brain samples measured with ComSLI. (**A-D**) **Human tongue muscle**. (**A**) Brightfield H&E image, 0.46µm/pixel; (1) epithelium, (2) stroma, (3) inner muscle layer. (**B**) Average scattering signal, 3µm/pixel. (**C**) ComSLI fiber orientation map, color-coded according to color wheel in (D). The insets show the fiber orientation distributions for the marked circular areas. (**D**) Zoomed-in area from (C) including different fiber layers; fiber orientations are displayed as colored lines for every 25th pixel. (**E-I**) **Human colorectal tissue**. (**E**) Brightfield H&E image, 0.46µm/pixel; (1) epithelium, (2) mucosa and submucosa, (3) circular muscle, (4) longitudinal muscle. (**F**) Average scattering signal, 3µm/pixel, with two blood vessels indicated by arrowheads. (**G**) ComSLI fiber orientation map, color-coded according to color wheel in (H). The insets show the fiber orientation distributions for the marked circular areas. Arrowheads indicate the basal membrane. (**H**,**I**) Upper and lower zoomed-in areas from (G); fiber orientations are displayed as colored lines for every 40th image pixel. Arrowheads indicate vertical and horizontal fiber orientations from circular and longitudinal muscle respectively (H), and blood vessels with fibers running circumferential (I). (**J-L**) **Human mandible**. (**J**) Brightfield H&E image, 0.46µm/pixel; (1) cortical bone on anterior side, (2) trabecular (cancellous) bone, (3) cortical bone on tooth side. (**K**) Average scattering signal, 3µm/pixel. (**L**) ComSLI fiber orientation map, color-coded according to color wheel. The insets show the fiber orientation distributions for the marked circular areas in the cortical bone. The arrowheads indicate spongy bone fiber orientations following the microstructure. (**M-O**) **Elastic artery wall**. (**M**) Brightfield elastin-stained image, 0.46µm/pixel. (**N**) Average scattering signal, 3µm/pixel. (**O**) ComSLI fiber orientation map. Highlighted are fiber layers with different directions going from lumenal to adventitial surfaces. The insets show the fiber orientation distributions for the entire layers at the position of the marked circular areas. All samples are 4µm-thin FFPE sections and stained with either H&E (tongue, colorectal, mandible) or elastin staining (artery wall).

Blood vessels yield high scattering signal (arrowheads in Fig. 5F), with collagen fibers wrapping around vessel walls (arrowheads in Fig. 5I).

In the mandible bone (Fig. 5J-L), the inner spongy (/trabecular) bone (2) shows fibers mostly following trabecular microstructure[36] (white arrowheads). The U-shaped cortical bone (1) shows a dominant fiber orientation in the direction of the force applied during mastication, i.e., from top left to bottom right (see corresponding insets 1a-c in Fig. 5L), while the superior region (3) exhibits more variable fiber orientations, distributing incoming loads to the rest of the jaw.

In the artery wall (Fig. 5M-O), ComSLI reveals microscopic arrangements of fibers in different layers. While the brightfield image (Fig. 5M) indicates the fiber type (pink area dominated by collagen fibers, dark/black area by elastin fibers, gray-green area by muscle fibers, indicated by arrowheads in corresponding color), the fiber orientation map (Fig. 5O) reveals distinct fiber directions in each layer, critical for artery mechanical properties[37]: fibers run mostly parallel to the surface in the inner (1), middle (3), and outer (5) layers; in the layers in between, the fibers run mostly (2) or also (4) perpendicular to the surface (see corresponding insets).

As in brain tissue, ComSLI reveals directed structures of non-brain tissues both for stained and unstained sections (Supplementary Fig. 13), and yields similar results across adjacent sections, for different section thicknesses (from 4µm to 15µm) and different steps of sample preparation, also for sections still in paraffin (Supplementary Fig. 13A,D,G).

Discussion

Nerve fibers form a dense network in the brain, determining its connectivity and function in health and disease. Here, we show that ComSLI retrieves microscopic fiber orientations across different species, diseases, and tissue types, in new and archived paraffin-treated tissue sections that were prepared with various stains and protocols at different steps of sample preparation. Such information would otherwise be undetectable with brightfield microscopy and inaccessible with other methods.

To enable detailed study of fiber trajectories, we presented novel analyses of the derived micron-resolution orientation maps. This included calculating the number of crossing fibers in the brain at multiple resolutions (Supplementary Fig. 1), whereby only 7% of white matter pixels showed crossings at 7µm resolution, which rises to ~95% for 1mm resolution, higher than previous estimates[27]. We also calculated microstructure-derived fiber orientation distributions (µFOD), enabling quantitative analyses and providing insights about the nerve fiber architecture at multiple resolutions. Combined with powerful tools adapted from MRI tractography[35,38,39], this also enabled tracing long-range axonal trajectories through the generation of orientation distribution functions (ODFs) and whole-brain and region-specific white and gray matter tractograms (e.g., Supplementary Fig. 2).

While scattered light imaging has previously revealed interwoven nerve fiber networks with high resolution[21–23], these studies were limited to unstained, cryo- or vibratome-sections where nerve fiber architecture could also be visualized with polarization microscopy, albeit with one fiber direction per pixel. In ComSLI, we use a directed rotating high-power LED spot (instead of an LED matrix display) for improved signal-to-noise ratio, allowing for the first time mapping of microscopic fiber architectures in various types of histological samples, including formalin-fixed paraffin-embedded (FFPE) and whole human brain sections like the *BigBrain* atlas (cf. Fig. 1). FFPE sections are commonly used in research and clinical laboratories, but their microscopic nerve fiber architecture cannot be analyzed with polarization microscopy due to a lack of birefringence (Supplementary Fig. 12).

Though previous work only studied healthy brain samples[21–23], we demonstrate here that ComSLI can provide novel information and valuable insights in neuropathology. By studying samples with diseases such as multiple sclerosis and leukoencephalopathy, we show that ComSLI, being robust to demyelination, can detect disturbed microarchitecture changes in lesions, and can also discern myelin from axonal loss, helping to differentiate lesion areas (Fig. 3). Moreover, taking advantage of the tractography analysis, ComSLI can reveal the loss of vulnerable pathways in degenerating brains, such as perforant fibers in a sclerotic and Alzheimer's Disease hippocampus (Supplementary Fig. 8). Thus, ComSLI can be applied to the study of multiple neurologic and psychiatric disorders with structural connectivity changes, such as Alzheimer's disease[40], Parkin-

son's disease[41], traumatic brain injury[42], stroke[43], multiple sclerosis[44], schizophrenia[45], epilepsy[46], or autism[47]. It can be used across any brain circuitry and can validate *ex vivo* diffusion MRI orientations[4], especially in areas with small or highly interwoven fiber tracts such as the hippocampus[20] or U-fibers[48], where sensitivity and high-resolution is key. Finally, it can be used to create reference maps of microscopic fiber architecture for entire brains, e.g., applied to and extending datasets such as the *BigBrain* atlas[11].

Finally, we applied our technique for the first time to non-brain samples – including muscle, bone and blood vessel tissues (Fig. 5 and Supplementary Fig. 13): ComSLI reveals not only nerve fiber architecture, but also other directed structures like collagen, muscle, and elastin fibers, which form intricate biological fiber networks that control mechanical and functional properties, and are altered in disease in muscle[49], connective[50–52], and epithelial[37,53] tissues. Our findings highlight the wide applicability of ComSLI, which can be used to reveal collagen[54], actin/myosin[55], elastin[56], or the (usually collagenous) fiber organization around tumors[57,58], which is related to staging and malignancy of the tumor, potentially allowing more accurate diagnosis and tailored cancer treatment.

The presented approach has the potential to make fiber mapping accessible to every laboratory: ComSLI is i) relatively low-cost, requiring only an LED spot, a sample stage, and a micron-resolution camera, ii) fast, with a full measurement performed within seconds, iii) compatible with sections prepared using virtually any protocol. In miniaturized form, using an LED-ring instead of a rotating LED, ComSLI can be an add-on to existing microscopes and easily be integrated into clinical workflows. This enables microscopic exploration of fiber orientations in health and disease on sections readily available in thousands of laboratories and clinics worldwide.

Regarding alternative approaches, we attempted to compare ComSLI to those that can provide fiber orientations for similar samples and scales. Structure tensor analysis was recently presented for reconstructing nerve fiber pathways in FFPE Nissl-stained brain sections (Nissl-ST)[25]. Compared to Nissl-ST, ComSLI provides significantly higher resolution in a label-free manner, including multiple crossing fiber orientations per image pixel (Fig. 4, Supplementary Figs. 10 and 11C), and the possibility for out-of-plane orientation information[21–23]. Diffusion MRI can image living human subjects tomographically but lacks cellular and microscopic details, which can help better define tracts and solve key tractography problems[59]. Compared to diffusion MRI, ComSLI provides much higher resolution leading to visualization of small fiber tracts invisible to MRI (Fig. 4 and Supplementary Fig. 10).

Our study has shown that ComSLI can be applied to various kinds of histological sections: FFPE, new or archived -even century-old, at different sample preparation stages, with various stains or section thicknesses - even to unstained sections still in paraffin (Supplementary Fig. 4),

or unfixed fresh-frozen sections (Supplementary Fig. 5). Together with previously shown applications on fixed cryo-sections[21] or vibratome sections[23], our study reveals the potential of ComSLI to reconstruct fiber organization in virtually any histology section in clinics or laboratories.

Given its independence from myelin birefringence, ComSLI can yield neuropathologic insights when combined with myelin-sensitive microscopic methods such as 3D-PLI[18–20], polarization-sensitive optical coherence tomography[16,17], or X-ray scattering[9,10,60,61]. Compared to 3D-PLI, which is the method-of-choice for micron-resolution fiber mapping on sections, ComSLI can be applied to various kinds of histological sections independent of sample preparation or birefringence, including FFPE sections, and can resolve crossing fibers per pixel, with an easy-to-implement and cost-effective setup.

Our study has some limitations. We only show in-plane fiber orientations, but the method also provides information of fiber inclination[21–23], and our future work will focus on quantifying out-of-plane angles. As light can scatter off any structure, imperfections on the microscope slide or coverslip (e.g., scratches or dust) will introduce artifacts. To this end, the slide should be cleaned (e.g., using wet cotton tips) before measurement, while unremovable scratches will introduce artifacts in the image that need to be excluded from analysis. While measurements were performed in transmission mode through thin sections, we aim to extend measurements to back-scattering mode to analyze fiber orientations on surfaces without sectioning. Finally, ComSLI provides fiber orientations without distinguishing between nerve, muscle, collagen, or other types of fibers. Future studies will investigate the different scattering signatures from distinct fiber types to enable label-free, multiplexed, fiber-specific analyses.

In conclusion, we have shown that ComSLI reveals the underlying fiber microarchitecture of tissues including paraffin-embedded formalin-fixed (FFPE) sections, independent of staining and birefringence, making it unique in revealing micron-resolution nerve fiber architecture in FFPE sections which are commonly used in laboratories world-wide. This fast, simple-to-implement, and cost-effective technique can become a routine tool to provide micrometer fiber orientation mapping of histological sections, opening new avenues in the investigation of the microarchitecture of tissues in health and disease.

Methods

Sample preparation

Whole human brain (BigBrain) sections

The silver-stained human brain section (Fig. 1, Supplementary Movie 1, and Supplementary Figs. 1, 2, and 10) was obtained from a 30-year-old, male body donor without neurological disorders. The brain was removed within 24 hours after death, fixed in 4% formaline, dehydrated in increasing alcohol series (80%, 90%, 96%, 100% ethanol for at least one week), and embedded in 57-60°C paraffin solution for two to three months. For a more detailed description, see Amunts et al., 2013[11]. Subsequently, the brain was coronally cut into 20 µm-thin sections from anterior to posterior with a large-scale microtome (Leica SM2500 Microtome) and mounted. The sections were placed in a decreasing alcohol series to remove the paraffin, stained with silver following the protocol of Merker[62] to highlight neuronal cell bodies, and mounted on glass slides. The sections are part of the so-called second *BigBrain* data set[63], 3D-reconstructed with the same spatial resolution of 20µm isotropic such as the original Jülich *BigBrain*s[11]. For our study, we used section no. 3452.

The Cresyl-violet stained human brain sections (Fig. 4, and Supplementary Figs. 8, 9, and 11) were obtained from a 71-year-old, male body donor without neurological disorders. The brain was prepared as described above, but stained with Cresyl-violet instead of silver. For our study, sections no. 3301 (Fig. 4, and Supplementary Figs. 8 and 9) and 2520 (Supplementary Fig. 11) were selected and measured one and a half years after tissue preparation.

The body donors gave written informed consent for the general use of postmortem tissue used in this study for aims of research and education. The usage is covered by a vote of the ethics committee of the medical faculty of the Heinrich Heine University Düsseldorf, Germany (#4863).

120-year-old myelin-stained human brain section

The myelin-stained human brain section (Fig. 2B) comes from the brain collection of the Cécile and Oskar Vogt Institute for Brain Research, Heinrich Heine University Düsseldorf, Germany. The brain of a 25-year-old male was embedded in celloidin and stained according to Weigert's iron hematoxylin myelin staining in 1904[64].

Human hippocampus, cortex, and pathology FFPE brain sections

Four-millimeter thick formalin-fixed human specimens were dehydrated in increasing ethanol steps (70% x2, 95% x2, 100% x3, 3.5hrs each step), cleared in xylene (3.5hrs x2), paraffin-embedded (3.5hrs x2), and sectioned into 5µm-thin sections. The sections were de-waxed and stained with agents as indicated. The hippocampal sections in Fig. 2A and Supplementary Fig. 3 were from an 89-year-old male with Alzheimer's pathology, stained against microglia (CD163), Perl's iron with Diaminobenzidine (DAB) enhancement, tau, and amyloid, with hematoxylin counterstain where indicated. Sections from brains with multiple sclerosis (80 years old, male,

from temporal periventricular white matter and cortex) and leukoencephalopathy (43 years old, male, from periventricular white matter and cingulum) were stained with hematoxylin and eosin, luxol fast blue plus hematoxylin and eosin, and neurofilament (2F11) (Fig. 3 and Supplementary Figs. 5-6). Hippocampal and visual cortex sections in Supplementary Fig. 4 were from a 60-year-old male stained with hematoxylin & eosin and a 67-year-old female stained with luxol fast blue respectively. The sclerotic hippocampal section in Supplementary Fig. 7 was from a 69-year-old female with epilepsy, the control was from a 66-year-old female with no neuropathologic abnormality, and the AD tau-stained hippocampus was the same as in Fig. 2A, as described above. Specimens were acquired under Stanford ADRC IRB (Assurance nr. FWA00000935).

Fresh-frozen human hippocampus and visual cortex sections

The human hippocampus and primary visual cortex fresh-frozen sections (Supplementary Fig. 5) were from an 88-year-old male with Lewy Body Disease, low Alzheimer's disease pathology, and cerebrovascular dementia. The brain was processed according to Stanford ADRC procedures; after autopsy, it was cut in 5mm coronal slabs and frozen using frozen metal plates in dry ice. The specimens were excised from the frozen slab, and 30µm sections were cut using a cryostat. The sections were uncoverslipped and let thaw under the microscope, which happened in the first ~100 seconds given their thickness. Specimens were acquired under Stanford ADRC IRB (Assurance nr. FWA00000935).

Mouse brain section

A female ~10-week-old C57BL/6 mouse (Jackson Laboratories) was housed in a temperature-controlled environment, with a 12-hour light/dark schedule and *ad libitum* food/water access. It was euthanized for the purposes of a different study (APLAC #32577) under anesthesia with 2-3% isoflurane followed by cardiac puncture and perfusion with 20mL phosphate buffered saline (PBS). The brain was harvested, kept in 4% paraformaldehyde (PFA) in PBS for 24 hours at 4ºC, transferred to 10%, 20%, and 30% sucrose in PBS, embedded in Tissue-Tek O.C.T. in dry ice for 1 hour, and cut sagittally into 10µm sections using a cryotome (Leica CM1860). The sections were subsequently washed, mounted on a glass slide, incubated with Iba1 antibody (dilution 1:200), secondary antibody (goat anti-rabbit Cy3 1:200), and cover-slipped. A mid-sagittal section was selected for evaluation (Fig. 2G-J).

Pig brain section

A 4-week female Yorkshire pig (#2) was euthanized for a different study (Stanford APLAC protocol nr 33684), the brain was harvested, cut into 5-mm coronal slabs using a brain slicer, and a mid-frontal slab (#5) was paraffin-embedded, similar to the human pathologic specimen preparation above. The slab was cut in 10µm sections using a Leica HistoCore AUTOCUT microtome. After deparaffinization, a section (#127) was stained with hematoxylin and eosin and cover-slipped (Fig. 2K-N).

Human tongue, colorectal, bone, and artery wall sections

The non-brain tissue sections (Fig. 5 and Supplementary Fig. 12) were obtained from a tissue archive at Erasmus Medical Center, Rotterdam, the Netherlands, approved by the Medisch Ethische Toetsing Commissie (METC) under number MEC-2023-0587. The tissue samples were obtained from patients during surgery. The bone sample was decalcified first using DecalMATE by Milestone Medical. Afterwards, all samples were fixed in 4% formaldehyde for 24 hours, dehydrated in increasing alcohol series (70%, 80%, 90%, 96%, 100% ethanol), treated with xylene, embedded in paraffin, and cut with a microtome (Leica RM2165) into 4µm-thin sections. The sections were placed in a decreasing alcohol series to remove the paraffin, mounted on glass slides, stained with hematoxylin and eosin (artery wall with Verhoeff-Van Gieson elastin staining), and then cover-slipped.

Brightfield microscopy

The whole human brain sections were scanned with the TissueScope LE120 Slide Scanner by Huron Digital Pathology, Huron Technologies International Inc. The device measures in brightfield mode with 20X magnification and 0.74 NA, providing a pixel size of 0.4µm. The final images were stored with a pixel size of 1µm.

The hippocampus, cortex, pathology, and animal brain sections were scanned using an Aperio AT2 whole slide scanner with the ImageScope software and a 20X magnification, resulting in brightfield images with a pixel size of 0.5µm.

The stained non-brain microscopy slides were scanned using the Nanozoomer 2.0 HT digital slide scanner by Hamamatsu Photonics K.K., offering a 20X magnification and a pixel size of 0.46µm. The unstained non-brain microscopy slides were scanned using the Keyence VHX-6000 Digital Microscope (with VH-ZST objective, 20X), with a pixel size of 10µm.

ComSLI

Whole human brain (silver-stained), hippocampus, cortex, pathology, and animal brain sections

Measurements were performed with a rotating light source and camera (cf. Fig. 1B), using a Flexacam C3 12 MP microscope camera (Leica) and a Navitar 12X Zoom Lens with a 0.67X Standard Adapter and a 0.5X Lens Attachment, with 4.25-9µm pixel size, as indicated in the figure captions. As light source, an ADJ Pinspot LED II was used, with 5.1cm diameter and 3.5o full-angle of divergence, oriented at ~45° with respect to the sample plane. A motorized specimen stage enabled the whole-human-brain section scanning in 8x5 tiles, all other brain sections were scanned at single tile. Images were acquired at 10o rotation steps (36 images/sample) with 125ms exposure time, except from the sections in paraffin that gave very strong scattering and were imaged with 7ms exposure time. Prior to the measurement, a 100mm diameter diffuser plate (Thorlabs) was measured for calibration (see below for calibration details).

Whole human brain (Cresyl-violet) and non-brain tissue sections

Measurements were similarly performed with a rotating light source and camera (cf. Fig. 1B), using a fiber-coupled LED light source consisting of an ultra-high power LED (UHP-FB-W50 by Prizmatix) with 400-750nm wavelength (peak at 443nm), 2-meter long step-index multimode silica (low OH) fiber patch cord (Thorlabs), a 25.4 mm diameter collimating optics (FCM1-0.5-CN by Prizmatix), and a 25.4 mm diameter engineered diffuser (beam shaper) for homogenizing the illumination (ED1-S20-MD by Thorlabs), yielding top-hat beam with 20° full-angle of divergence. The exposure time was adjusted manually per sample for maximizing the dynamic range of the captured signal while avoiding saturation (range: 50-100 ms). The light source was oriented at ~45° with respect to the sample and rotated with a motorized specimen stage (ZABER X-RSB060AD-E01-KX14A) in steps of 15° (24 images/sample). Images were taken with a 20 MP monochromatic CMOS camera (BASLER acA5472-17um) and a Rodenstock Apo-Rodagon-D120 Lens, yielding a pixel size of 3µm (4µm optical resolution) and a field-of-view of 16x11mm². A motorized specimen stage was used to perform whole-slide scanning. Prior to the measurement, a diffuser plate (DG100x100 N-BK7 ground glass diffuser, 1500 grit, Thorlabs) was measured for calibration.

120-year-old myelin-stained brain section

The measurement was performed with a similar camera and lens as for the non-brain tissue sections (BASLER acA5472-17uc and Rodenstock Apo-Rodagon-D120), using an LED display instead of a focused light source (50x50cm², 128x128 RGB-LEDs, Absen Polaris 3.9pro In/Outdoor LED Cabinet). The sample was illuminated by a green circle segment (9° azimuthal and polar widths, respectively) with an effective illumination angle of 47°, which was rotated in 15° steps. Images were taken with 10 seconds exposure time and a gain of 10, and 4 images were averaged per illumination angle to increase signal to noise.

ComSLI image analysis

Flat-field correction

Prior to each measurement session, a diffuser plate was measured under similar conditions. A 100-pixel Gaussian blur was applied to diffuser images to homogenize defects. Subsequently, the blurred images of all angles were divided by the average of their maxima for normalization. These normalized diffuser images were used to calibrate the measured tissue images, aiming to account for the uneven illumination across the field of view for each image: Each tissue image was divided by its corresponding normalized diffuser image of the same illumination angle.

Generation of fiber orientation and vector maps

Each calibrated image series from a ComSLI measurement was evaluated with the open-source software SLIX[34], which analyzes the position of scattering peaks to compute the fiber orientations and visualize them in in color-encoded maps, using multi-colored pixels and colored vector

lines. Measurements with 15° azimuthal steps were processed without filtering. Measurements with 10° azimuthal steps were processed with Fourier low pass filter (40% cutoff frequency, 0.225 window width) before generating the parameter maps, as described in [22].

Microstructure-derived fiber orientation distributions (μFODs)

To calculate and plot the μFODs, the ComSLI fiber orientation map was partitioned into pixel kernels depending on the intended μFOD resolution. For instance, for a ComSLI dataset with pixel size of 7μm and intended μFOD resolutions of ~50 or ~500μm, a 7x7 or 71x71 pixel kernel was used respectively (Fig. 1H). Similarly, to calculate μFODs for specific regions of interest, e.g., the lesions in pathology (Fig. 3), orientations of all pixels in the area were considered. All fiber orientations of all pixels within each kernel or area or interest were then rendered as a polar histogram in 20 bins of 9°, covering 0° -180°, and mirrored to 180° -360°. To create a continuous polar function representing the μFOD, the mid-points of the bins were fitted by a spline, which was then rendered as polar plot (Fig. 1H, Fig. 3D,G,X, Fig. 4C,D, Fig. 5C,G,L,O).

Diffusion MR-based orientation distribution functions (ODFs) and tractography

To generate ODFs and enable tractography, we opted for using existing tools developed in MR tractography, given the advanced and widely tested algorithms used in the field. To achieve that, an artificial diffusion MRI dataset was created based on the ComSLI μFODs described above. The dataset included 3 b=0ms/μm^2 and 60 b=1ms/μm^2 volumes. The 3 b=0ms/μm^2 volumes had a value of 1 at all voxels. The 60 b=1ms/μm^2 volumes consisted of 3 sets: **i**) The first 20 were derived for the 20 in-plane orientations of the μFOD angles (20 angles, 9° apart covering 180°), see above. There, the signal for each angle was calculated for every pixel as $e^{-n/10}$, where *n* is the frequency of fiber orientations for that angle in that pixel, based on the μFOD polar histogram. **ii**) The second 20 orientations were at the plane perpendicular to the plane of the section. For these, the signal was set to 1 for all pixels, indicating no signal loss and hence no axons along that plane, thus enforcing the orientations to be within the section plane. **iii**) The third set of 20 orientations was the initial set of 20 polar histogram orientations but tilted 20° off the section plane towards the perpendicular plane. There, each pixel's signal was $1-\frac{1-Signal_0}{5}$, where $Signal_0$ is the signal of the first set of angles. This aimed to approximate a diffusion MRI signal and fiber distribution off-plane, where the signal loss at 20° off the detected in-plane axon orientation is 20% of the signal loss along the axons.

To compute the ODFs and tractograms, *MRtrix3*[35] functions were used with the generated artificial MRI signal along with the corresponding bval and bvec files as input: *dwi2response* with the *fa* algorithm and l_{max}=6 to calculate the fiber response and *dwi2fod* with the *csd* algorithm and l_{max}=6 to calculate the ODFs. Finally, the *tckgen* function was used to generate tractograms, with a minimum tract length of 2mm, which was found to be reasonable to compute given the micron-scale pixel sizes.

696 **Nissl-ST**

The fiber orientation maps were computed in Matlab following the procedure described and code
698 shared by Schurr & Mezer[25], using default settings and 100µm as kernel to compute the structure tensor (effective resolution).

700 **ComSLI – Histology registration**

To enable quantitative, pixel-wise comparison between ComSLI and Nissl-ST outputs (Fig. 4
702 and Supplementary Figs. 10-11) as well as quantification of the ComSLI and histology stain intensities (Fig. 3 and Supplementary Fig. 6), the histology images were linearly 2D-registered to
704 the corresponding ComSLI average scattering images of the same section using the *antsRegistration* function in *ANTs*[65] (options: *--transform Similarity[0.1], --convergence [100 x 70 x 50 x*
706 *0,1e-6,10] --smoothing-sigmas 3x2x1x0vox --shrink-factors 8x4x2x1*).

To register consecutive histology sections (Figs. 2, 3, and Supplementary Fig. 6) the *SyN* trans-
708 form of the same *ANTs* command was used (options: *--transform SyN[0.1,3,0] --convergence [800 x 400 x 200 x 100 x 70 x 50 x 0,1e-6,10] --smoothing-sigmas 15x9x5x3x2x1x0vox --shrink-*
710 *factors 64x32x16x8x4x2x1*).

3D-PLI

712 The 3D-PLI measurements were performed using the LMP3D microscope (Taorad GmbH, Germany), containing an evo4070MFLGEC (2048x2048) camera and a Nikon 4x (NA 0.2) lens,
714 which achieves a pixel size of 1.85µm and an in-plane optical resolution of 2.2µm (determined by US-Airforce target). The sample was illuminated by linearly polarized light in 20° rotation
716 angles and analyzed by a circular analyzer as described by Axer et al.[19]. 3D-PLI FOM was computed on the supercomputer JURECA at Forschungszentrum Jülich (grant no. 28954).

718 **Diffusion MRI**

The diffusion MRI dataset[30] is from a 30 year-old male who underwent 18 hours of diffusion
720 MRI scanning in the MGH-USC 3T Connectom scanner using gSlider-SMS[66]. After manually identifying the MR plane that most closely matched the *BigBrain* histology sections, the entire
722 dataset was rotated using FreeSurfer's *freeview* and the b-vectors were rotated at the same angles (rotation angles for the Silver-stained section were -34° sagittal and 1.5° axial, for the Cresyl-vio-
724 let -30.4° sagittal). Fiber responses and orientation distributions were computed using the *dwi2response* and *dwi2fod* functions in *MRtrix3*[35], using the multi-tissue, multi-shell algorithm[38],
726 and visualized in *mrview*. To generate whole-brain colormaps in Fig. 4 and Supplementary Fig. 10, *MRtrix3*'s *sh2amp* function was used to probe fiber orientations at the coronal plane at 5° in-
728 tervals, and colormaps were generated using SLIX[34].

Data availability

All data underlying the study and the original image files are available in the data repository Dryad: https://doi.org/10.5061/dryad.02v6wwqb2.

Code availability

The initial flat-field correction of raw ComSLI images was performed with custom MATLAB code as described in the respective section. The ComSLI fiber orientation maps were generated with the open-source software *SLIX,* available on GitHub (https://github.com/3d-pli/SLIX/). The Nissl-ST fiber orientation maps were generated in MATLAB using code shared by Schurr & Mezer[25]. The MRI orientation distribution functions (ODFs) were computed with the open-source software *MRtrix3* which is available on GitHub (https://github.com/MRtrix3/) and visualized with the tool *mrview*. The MATLAB code to generate µFODs from ComSLI orientation maps, create a virtual diffusion MRI dataset, and generate ODFs and tractography using MR tools, is provided together with data in the Dryad repository, including a sample whole-brain dataset.

Abbreviations

3D-PLI: three-dimensional polarized light imaging
AD: Alzheimer's disease
CA1-3: cornu ammonis 1-3
ComSLI: computational scattered light imaging
dMRI: diffusion magnetic resonance imaging
FFPE: formalin-fixed paraffin-embedded
gm: gray matter
H&E: hematoxylin and eosin
LFB: luxol fast blue
MRI: magnetic resonance imaging
µFOD: microstructure-informed fiber orientation distribution
Nissl-ST: Nissl-based structure tensor
nwm: normal white matter
ODF: orientation distribution function
PBS: phosphate buffered saline
PFA: paraformaldehyde
SAXS: small angle X-ray scattering
SLI: scattered light imaging

References

1. Sporns, O., Tononi, G. & Kötter, R. The human connectome: a structural description of the human brain. *PLoS Comput Biol* **1**, e42–e42 (2005).
2. Axer, M. & Amunts, K. Scale matters: The nested human connectome. *Science* **378**, 500–504 (2022).
3. Jeurissen, B., Descoteaux, M., Mori, S. & Leemans, A. Diffusion MRI fiber tractography of the brain. *NMR in Biomedicine* **32**, e3785–e3785 (2019).
4. Yendiki, A. *et al.* Post mortem mapping of connectional anatomy for the validation of diffusion MRI. *NeuroImage* **256**, 119146–119146 (2022).
5. Loomba, S. *et al.* Connectomic comparison of mouse and human cortex. *Science* **377**, eabo0924–eabo0924 (2023).
6. Xu, C. S. *et al.* An open-access volume electron microscopy atlas of whole cells and tissues. *Nature* **599**, 147–151 (2021).
7. Eberle, A. L. & Zeidler, D. Multi-Beam Scanning Electron Microscopy for High-Throughput Imaging in Connectomics Research. *Frontiers in Neuroanatomy* **12**, (2018).
8. Salo, R. A. *et al.* Quantification of anisotropy and orientation in 3D electron microscopy and diffusion tensor imaging in injured rat brain. *NeuroImage* **172**, 404–414 (2018).
9. Georgiadis, M. *et al.* Imaging crossing fibers in mouse, pig, monkey, and human brain using small-angle X-ray scattering. *Acta Biomaterialia* **164**, 317–331 (2023).
10. Georgiadis, M. *et al.* Nanostructure-specific X-ray tomography reveals myelin levels, integrity and axon orientations in mouse and human nervous tissue. *Nature Communications* **12**, (2021).
11. Amunts, K. *et al.* BigBrain: An Ultrahigh-Resolution 3D Human Brain Model. *Science* **340**, 1472–1475 (2013).
12. Pellicciari, C., Biggiogera, M., & Pellicciari. *Histochemistry of Single Molecules*. (Springer, 2017).
13. Costantini, I. *et al.* Autofluorescence enhancement for label-free imaging of myelinated fibers in mammalian brains. *Scientific Reports* **11**, 8038 (2021).
14. Khan, A. R. *et al.* 3D structure tensor analysis of light microscopy data for validating diffusion MRI. *NeuroImage* **111**, 192–203 (2015).
15. Wang, H., Lenglet, C. & Akkin, T. Structure tensor analysis of serial optical coherence scanner images for mapping fiber orientations and tractography in the brain. *J Biomed Opt* **20**, 036003 (2015).

16. Wang, H. *et al.* as-PSOCT: Volumetric microscopic imaging of human brain architecture and connectivity. *NeuroImage* **165**, 56–68 (2018).
17. Liu, C. J. *et al.* Refractive-index matching enhanced polarization sensitive optical coherence tomography quantification in human brain tissue. *Biomedical Optics Express* **13**, 358–372 (2022).
18. Axer, M. *et al.* A novel approach to the human connectome: Ultra-high resolution mapping of fiber tracts in the brain. *NeuroImage* **54**, 1091–1101 (2011).
19. Axer, M. *et al.* High-resolution fiber tract reconstruction in the human brain by means of three-dimensional polarized light imaging. *Frontiers in neuroinformatics* **5**, 34–34 (2011).
20. Zeineh, M. M. *et al.* Direct Visualization and Mapping of the Spatial Course of Fiber Tracts at Microscopic Resolution in the Human Hippocampus. *Cereb Cortex* **27**, 1779–1794 (2017).
21. Menzel, M. *et al.* Scattered Light Imaging: Resolving the substructure of nerve fiber crossings in whole brain sections with micrometer resolution. *NeuroImage* **233**, 117952–117952 (2021).
22. Menzel, M. *et al.* Scatterometry Measurements With Scattered Light Imaging Enable New Insights Into the Nerve Fiber Architecture of the Brain. *Frontiers in Neuroanatomy* **15**, (2021).
23. Menzel, M., Gräßel, D., Rajkovic, I., Zeineh, M. M. & Georgiadis, M. Using light and X-ray scattering to untangle complex neuronal orientations and validate diffusion MRI. *eLife* **12**, e84024 (2023).
24. Sanderson, T., Wild, G., Cull, A. M., Marston, J. & Zardin, G. 19—Immunohistochemical and immunofluorescent techniques. *Bancroft's Theory and Practice of Histological Techniques, 8th ed.; Suvarna, SK, Layton, C., Bancroft, JD, Eds* 337–394 (2018).
25. Schurr, R. & Mezer, A. A. The glial framework reveals white matter fiber architecture in human and primate brains. *Science* **374**, 762–767 (2021).
26. Menzel, M. *et al.* Toward a High-Resolution Reconstruction of 3D Nerve Fiber Architectures and Crossings in the Brain Using Light Scattering Measurements and Finite-Difference Time-Domain Simulations. *Physical Review X* **10**, 21002–21002 (2020).
27. Jeurissen, B., Leemans, A., Tournier, J. D., Jones, D. K. & Sijbers, J. Investigating the prevalence of complex fiber configurations in white matter tissue with diffusion magnetic resonance imaging. *Hum Brain Mapp* **34**, 2747–2766 (2013).
28. Schilling, K. G. *et al.* Histological validation of diffusion MRI fiber orientation distributions and dispersion. *NeuroImage* **165**, 200–221 (2018).

29. Schmahmann D.N., J. D. P., Schmahmann, J. D. & Pandya, D. N. *Fiber Pathways of the Brain*. (Oxford University Press, New York, 2006).

30. Wang, F. *et al.* In vivo human whole-brain Connectom diffusion MRI dataset at 760 µm isotropic resolution. *Scientific Data* **8**, 122 (2021).

31. Plantinga, B. R. *et al.* Ultra-High Field MRI Post Mortem Structural Connectivity of the Human Subthalamic Nucleus, Substantia Nigra, and Globus Pallidus. *Frontiers in Neuroanatomy* **10**, (2016).

32. Leist, D. P., Nettleton, G. S. & Feldhoff, R. C. Determination of lipid loss during aqueous and phase partition fixation using formalin and glutaraldehyde. *J Histochem Cytochem* **34**, 437–441 (1986).

33. Kirschner, D. A. & Hollingshead, C. J. Processing for electron microscopy alters membrane structure and packing in myelin. *Journal of Ultrastructure Research* **73**, 211–232 (1980).

34. Reuter, J. A. & Menzel, M. SLIX: A Python package for fully automated evaluation of Scattered Light Imaging measurements on brain tissue. *Journal of Open Source Software* **5**, 2675–2675 (2020).

35. Tournier, J.-D. *et al.* MRtrix3: A fast, flexible and open software framework for medical image processing and visualisation. *NeuroImage* **202**, 116137 (2019).

36. Georgiadis, M. *et al.* Ultrastructure organization of human trabeculae assessed by 3D sSAXS and relation to bone microarchitecture. *PLoS One* **11**, e0159838–e0159838 (2016).

37. Gasser, T. C., Ogden, R. W. & Holzapfel, G. A. Hyperelastic modelling of arterial layers with distributed collagen fibre orientations. *Journal of The Royal Society Interface* **3**, 15–35 (2005).

38. Jeurissen, B., Tournier, J.-D., Dhollander, T., Connelly, A. & Sijbers, J. Multi-tissue constrained spherical deconvolution for improved analysis of multi-shell diffusion MRI data. *NeuroImage* **103**, 411–426 (2014).

39. Tournier, J. D., Calamante, F. & Connelly, A. Robust determination of the fibre orientation distribution in diffusion MRI: Non-negativity constrained super-resolved spherical deconvolution. *NeuroImage* **35**, 1459–1472 (2007).

40. Filippi, M. *et al.* Changes in functional and structural brain connectome along the Alzheimer's disease continuum. *Molecular Psychiatry* **25**, 230–239 (2020).

41. Yang, Y. *et al.* Alteration of brain structural connectivity in progression of Parkinson's disease: A connectome-wide network analysis. *NeuroImage: Clinical* **31**, 102715 (2021).

42. Raizman, R. *et al.* Traumatic Brain Injury Severity in a Network Perspective: A Diffusion MRI Based Connectome Study. *Scientific Reports* **10**, 9121 (2020).

43. Paul, T. *et al.* Interhemispheric Structural Connectivity Underlies Motor Recovery after Stroke. *Annals of Neurology* **94**, 785–797 (2023).
44. Pagani, E. *et al.* Structural connectivity in multiple sclerosis and modeling of disconnection. *Mult Scler* **26**, 220–232 (2020).
45. Yao, B., Neggers, S. F. W., Kahn, R. S. & Thakkar, K. N. Altered thalamocortical structural connectivity in persons with schizophrenia and healthy siblings. *NeuroImage: Clinical* **28**, 102370 (2020).
46. Royer, J. *et al.* Epilepsy and brain network hubs. *Epilepsia* **63**, 537–550 (2022).
47. Valenti, M. *et al.* Abnormal Structural and Functional Connectivity of the Corpus Callosum in Autism Spectrum Disorders: a Review. *Review Journal of Autism and Developmental Disorders* **7**, 46–62 (2020).
48. Movahedian Attar, F. *et al.* Mapping Short Association Fibers in the Early Cortical Visual Processing Stream Using In Vivo Diffusion Tractography. *Cerebral Cortex* **30**, 4496–4514 (2020).
49. Purslow, P. P. & Trotter, J. A. The morphology and mechanical properties of endomysium in series-fibred muscles: variations with muscle length. *Journal of Muscle Research & Cell Motility* **15**, 299–308 (1994).
50. Rho, J.-Y., Kuhn-Spearing, L. & Zioupos, P. Mechanical properties and the hierarchical structure of bone. *Medical Engineering & Physics* **20**, 92–102 (1998).
51. Stockhausen, K. E. *et al.* Collagen Fiber Orientation Is Coupled with Specific Nano-Compositional Patterns in Dark and Bright Osteons Modulating Their Biomechanical Properties. *ACS Nano* **15**, 455–467 (2021).
52. Liebi, M. *et al.* Nanostructure surveys of macroscopic specimens by small-angle scattering tensor tomography. *Nature* **527**, 349–352 (2015).
53. Corr, D. T. & Hart, D. A. Biomechanics of Scar Tissue and Uninjured Skin. *Advances in Wound Care* **2**, 37–43 (2013).
54. Lin, J. *et al.* Mechanical Roles in Formation of Oriented Collagen Fibers. *Tissue Engineering Part B: Reviews* **26**, 116–128 (2020).
55. Weirich, K. L., Stam, S., Munro, E. & Gardel, M. L. Actin bundle architecture and mechanics regulate myosin II force generation. *Biophys J* **120**, 1957–1970 (2021).
56. Baumann, L. *et al.* Clinical Relevance of Elastin in the Structure and Function of Skin. *Aesthetic Surgery Journal Open Forum* **3**, ojab019 (2021).
57. Han, W. *et al.* Oriented collagen fibers direct tumor cell intravasation. *Proceedings of the National Academy of Sciences* **113**, 11208–11213 (2016).

58. Despotović, S. Z. *et al.* Altered organization of collagen fibers in the uninvolved human colon mucosa 10 cm and 20 cm away from the malignant tumor. *Scientific Reports* **10**, 6359 (2020).

59. Zhu, S. *et al.* Imaging the structural connectome with hybrid MRI-microscopy tractography. *Medical Image Analysis* 103498 (2025) doi:10.1016/j.media.2025.103498.

60. Georgiadis, M. *et al.* 3D scanning SAXS: A novel method for the assessment of bone ultrastructure orientation. *Bone* **71**, 42–52 (2015).

61. Georgiadis, M. *et al.* Retrieving neuronal orientations using 3D scanning SAXS and comparison with diffusion MRI. *NeuroImage* **204**, 116214–116214 (2020).

62. Merker, B. Silver staining of cell bodies by means of physical development. *Journal of Neuroscience Methods* **9**, 235–241 (1983).

63. Mohlberg, H., Tweddell, B., Lippert, T. & Amunts, K. Workflows for Ultra-High Resolution 3D Models of the Human Brain on Massively Parallel Supercomputers. in *International Workshop on Brain-Inspired Computing* (2015).

64. Vogt, O. Die myelogenetische Gliederung des Cortex cerebelli. *J. Psychol. Neurol* **5**, 250–253 (1905).

65. Avants, B., Epstein, C., Grossman, M. & Gee, J. Symmetric diffeomorphic image registration with cross-correlation: Evaluating automated labeling of elderly and neurodegenerative brain. *Medical Image Analysis* **12**, 26–41 (2008).

66. Setsompop, K. *et al.* High-resolution in vivo diffusion imaging of the human brain with generalized slice dithered enhanced resolution: Simultaneous multislice (gSlider-SMS). *Magnetic Resonance in Medicine* **79**, 141–151 (2018).

Acknowledgments

We thank Markus Cremer and the laboratory team at Forschungzentrum Jülich (INM-1), Germany, for preparing the whole human brain (*BigBrain*) sections, and Philipp Schlömer for performing and processing the 3D-PLI measurement. We thank David Camarillo for his help with the pig project. This work was supported by the National Institutes of Health grant nos. R03AG083702 (M.G.), R01MH092311 (K.A.), R01AG061120 (M.Z.), and R21AG072675 (M.Z.). F.H., K.A., M.A. and M.M. received funding from the European Union's Horizon 2020 Research and Innovation Programme grant no. 945539 ("Human Brain Project" SGA3) and no. 101147319 ("EBRAINS 2.0 Project"). F.H., L.E. and M.M. received funding from the Deutsche Forschungsgemeinschaft (DFG) Project no. 498596755. M.M. received funding from the Klaus Tschira Boost Fund and from the Helmholtz Association's Initiative and Networking Fund through the Helmholtz International *BigBrain* Analytics and Learning Laboratory (HIBALL) under the Helmholtz International Lab grant agreement InterLabs-0015. H.A. received funding from the Convergence Imaging Facility and Innovation Center (CIFIC) of TU Delft, Erasmus MC, and Erasmus UR. M.C. received funding from the National Institutes of Health F31 award number 1F31AG077905. M.G. received funding from the Foundation of the American Society of Neuroradiology, and the Alzheimer's Association Research Fellowship no. 24AARF-1241479.

Author contributions

M.G. and M.M. co-designed the study, developed the LED-spot setup, supervised the research, analyzed and interpreted the data, prepared the figures, and wrote the first version of the manuscript. M.G. conducted ComSLI brain measurements except for the 120-year-old and the whole human brain (cresyl violet) sections, and performed quantitative analyses including the μFODs, multi-modal comparisons, MR-inspired ODFs and tractography. F.H. optimized the measurement parameters and hardware of the LED-display setup, performed first measurements of the FFPE whole brain sections, measured and analyzed the myelin-stained human brain section, and designed the ComSLI setup sketch. H.A. measured and analyzed the non-brain tissue samples and prepared the corresponding figures. L.E. measured and analyzed the Cresyl-violet stained, whole human brain sections. J.N. contributed to the design of the pathology study, provided anatomical analysis and interpretation of the brain pathology samples. H.M.T. helped with the Nissl-ST analysis. M.W. performed initial measurements of FFPE sections. A.L. contributed to scanning of the silver-stained whole human brain section, W.H.D.H. helped with setting up the measurements with the LED-spot, and M.C. contributed to the mouse brain study. M.D. provided anatomical analysis and interpretation of tongue, jar bone, and blood vessel samples, S.A.K. of colorectal samples, S.K. of oral tissue samples, and R.A.S. of pathological human brain samples. K.S. and C.L. helped design the comparison to dMRI, and C.L with analyzing the dMRI data set. K.A. provided the *BigBrain* sections, contributed to the anatomical content and participated in the design of the study. M.A. and M.Z. co-designed the study and contributed to data interpretation and supervision. All authors contributed to revision and editing of the manuscript.

Competing interests

The authors declare no competing interests.

Additional information

Supplementary information accompanies this paper.

Correspondence and requests for materials should be addressed to M.G. or M.M.

Supplementary Information

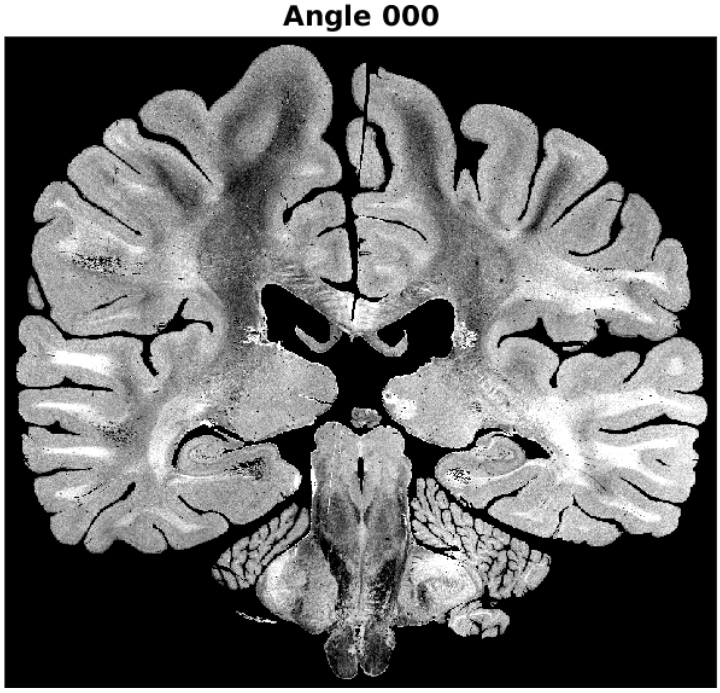

Supplementary Movie 1 | ComSLI dataset of whole human brain *BigBrain* section (second *BigBrain* dataset, section no. 3452, FFPE, silver-stained, fiber orientations in main Fig. 1). Each frame shows pixel intensities after calibration (see Methods) for the entire brain at each illumination angle φ (in degrees). The movie, which has been 5x downsampled to reduce its size of many gigabytes, can be downloaded from the data repository Dryad: https://doi.org/10.5061/dryad.02v6wwqb2 [SupplementaryMovie1.gif].

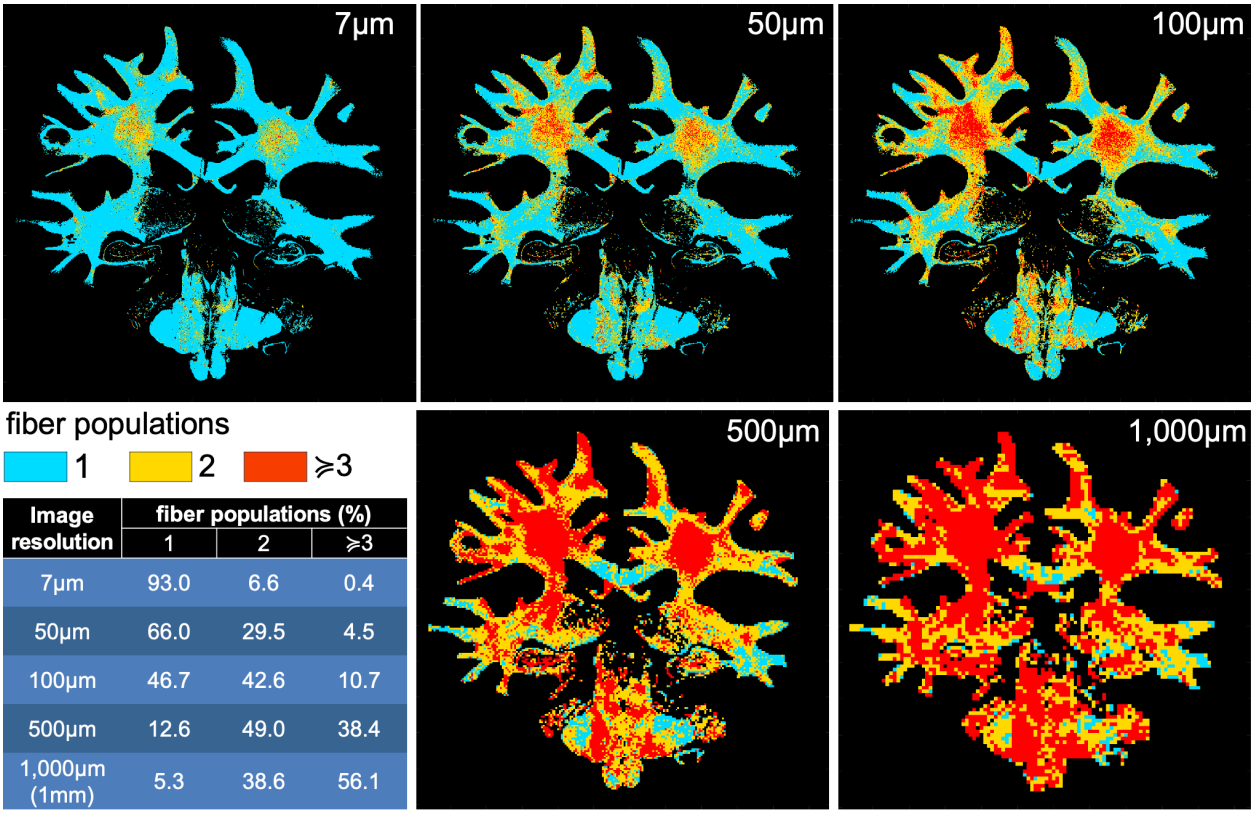

Image resolution	fiber populations (%)		
	1	2	⩾3
7µm	93.0	6.6	0.4
50µm	66.0	29.5	4.5
100µm	46.7	42.6	10.7
500µm	12.6	49.0	38.4
1,000µm (1mm)	5.3	38.6	56.1

Supplementary Fig. 1 | Number of fiber populations at different pixel sizes. Maps of the number of fiber populations with different orientations per pixel, for various pixel sizes, starting for single pixels at the ComSLI resolution for this experiment (7µm), then pixel kernels of 7x7 pixels (~50µm), 14x14 pixels (~100µm), 71x71 pixels (~500µm), and 143x143 pixels (~1mm).

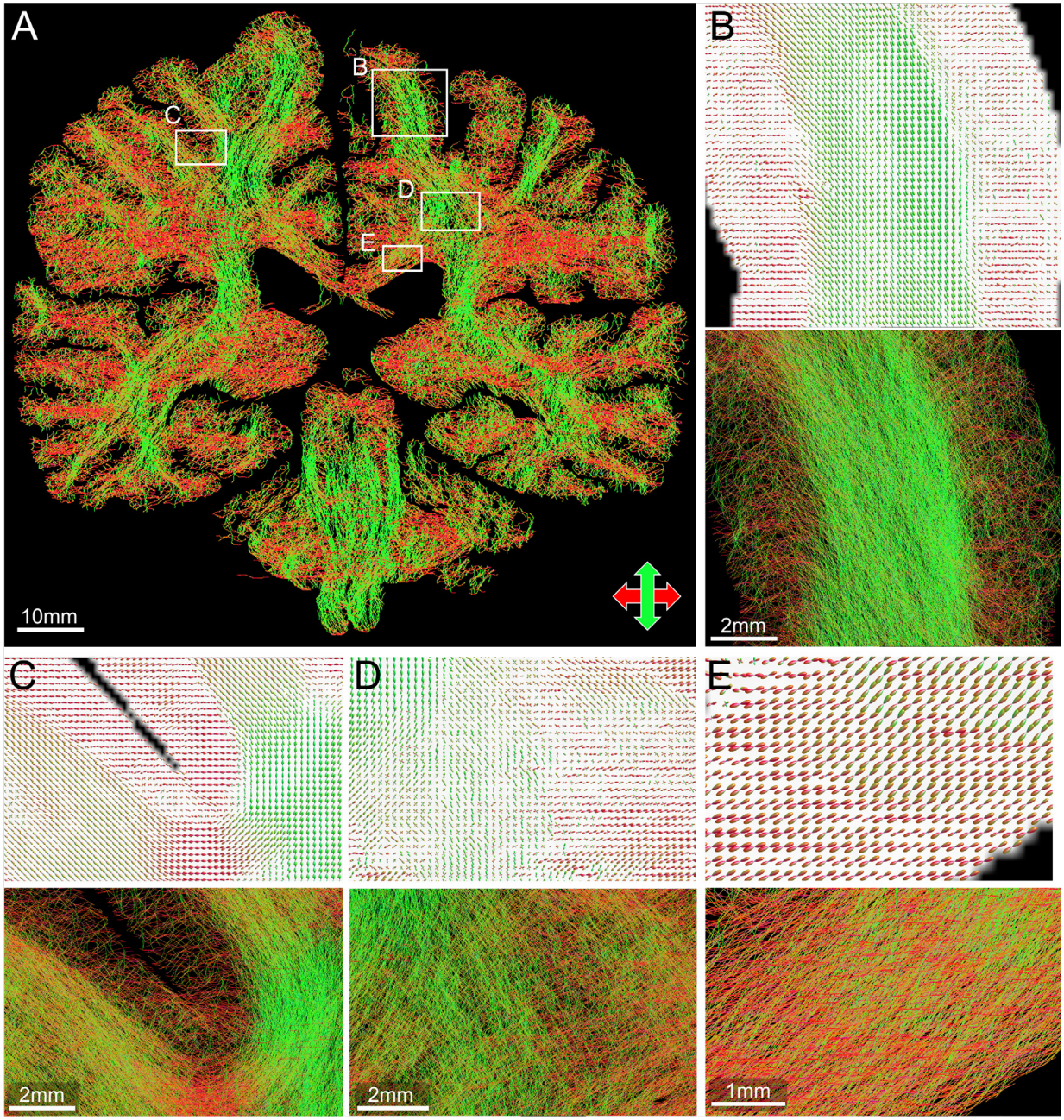

Supplementary Fig. 2 | Microstructure-based orientation distribution functions (ODFs) and whole-brain tractography. (**A**) Tractogram of the whole brain based on ComSLI microscopic fiber orientations for section no. 3452 from the second *BigBrain* dataset, FFPE, silver-stained (same as in main text Fig. 1). (**B-E**) ODFs and tracts for the boxes marked in A. (**B**) ODFs and tracts for a white and gray matter region of the precentral gyrus, where very dense fiber tracts dominate the white matter reflecting the strong, almost unidirectional ODFs, with abundant fibers in the gray matter areas too, mostly following the cortical columns, with some also running across them. (**C**) ODFs and tracts for a white and gray matter region including pre/post-central gyrus U-fibers, with some fibers also connecting into gray matter. (**D**) ODFs and tracts for a part of the corona radiata, with hundreds of fibers seen crossing. (**E**) ODFs and tracts for a part of the corpus callosum, with mostly unidirectional ODFs resulting in fibers running superolaterally. ODFs correspond to microstructure-based fiber orientation distributions (μFODs) of 30×30 pixels (210×210μm^2).

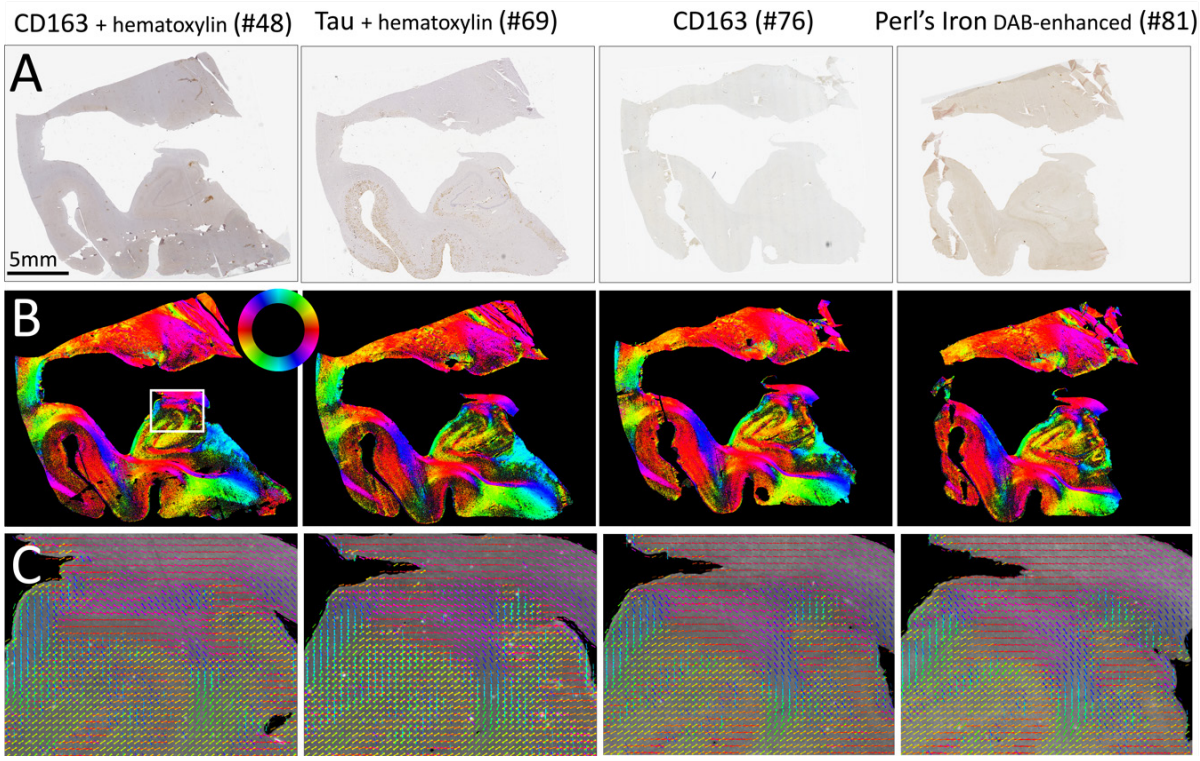

Supplementary Fig. 3 | Differently stained FFPE sections of a human hippocampus measured with ComSLI (same block as in main Fig. 2A-C). (**A**) Brightfield microscopy images, 0.5µm/pixel. (**B**) Color-coded fiber orientation maps from ComSLI, 7µm/pixel. (**C**) Zoomed-in fiber orientation vectors (rectangular region marked by white box in (B)). Vectors of kernels of 15x15 pixels are overlaid for visual clarity.

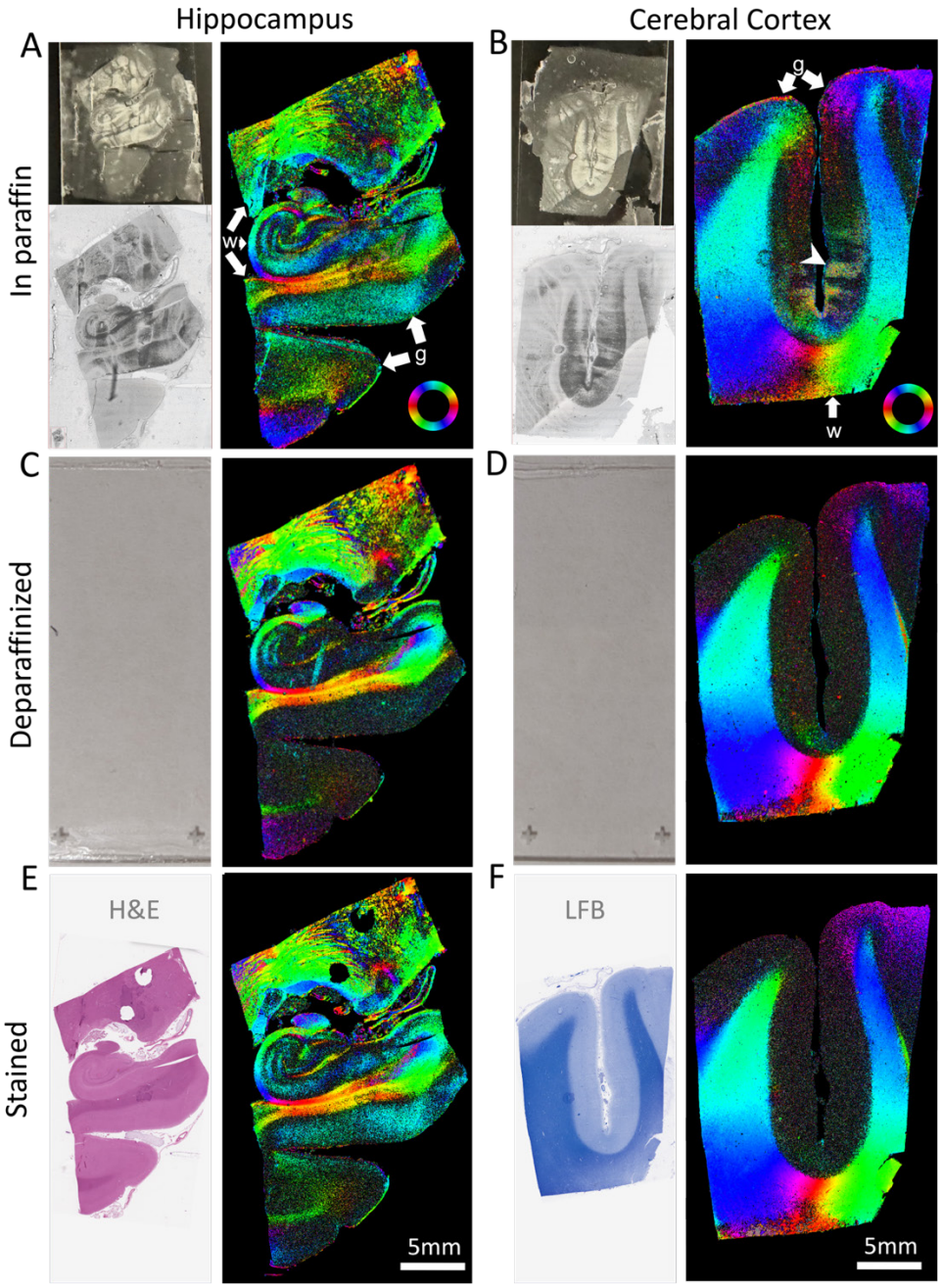

Supplementary Fig. 4 | ComSLI at different steps of FFPE sample preparation. Left: human hippocampus, right: human isocortex and subcortical white matter. Each panel contains brightfield images, 0.5µm/pixel (left side) and the respective ComSLI color-coded fiber orientations, 8µm/pixel (right side). (**A,B**) Sections still in paraffin. The fiber orientations are clearly visible in white (w) and gray (g) matter, despite evident paraffin structures in the photographs (top left corner) and slide-scanned images (bottom left corner). Small folds in the physical section create small artifacts in the gray matter (arrowhead in (B)). (**C,D**) The same sections after deparaffinization, before staining. The sections lack brightfield contrast for slide-scanning so only photographs are shown (left). Retrieved fiber orientations are similar to those in (A,B), especially in the white matter. (**E,F**) The same sections after staining (hippocampus: hematoxylin and eosin (H&E), cortex: luxol fast blue (LFB)), where orientations follow the same orientation patterns. Overall, gray matter orientations are more pronounced in paraffinized compared to unstained sections. In the hippocampus, gray matter orientations were pronounced in the stained section as well, similar to the hippocampi in main Fig. 2 and Supplementary Fig. 3, owing to the multiple tracts crossing the hippocampal gray matter[20].

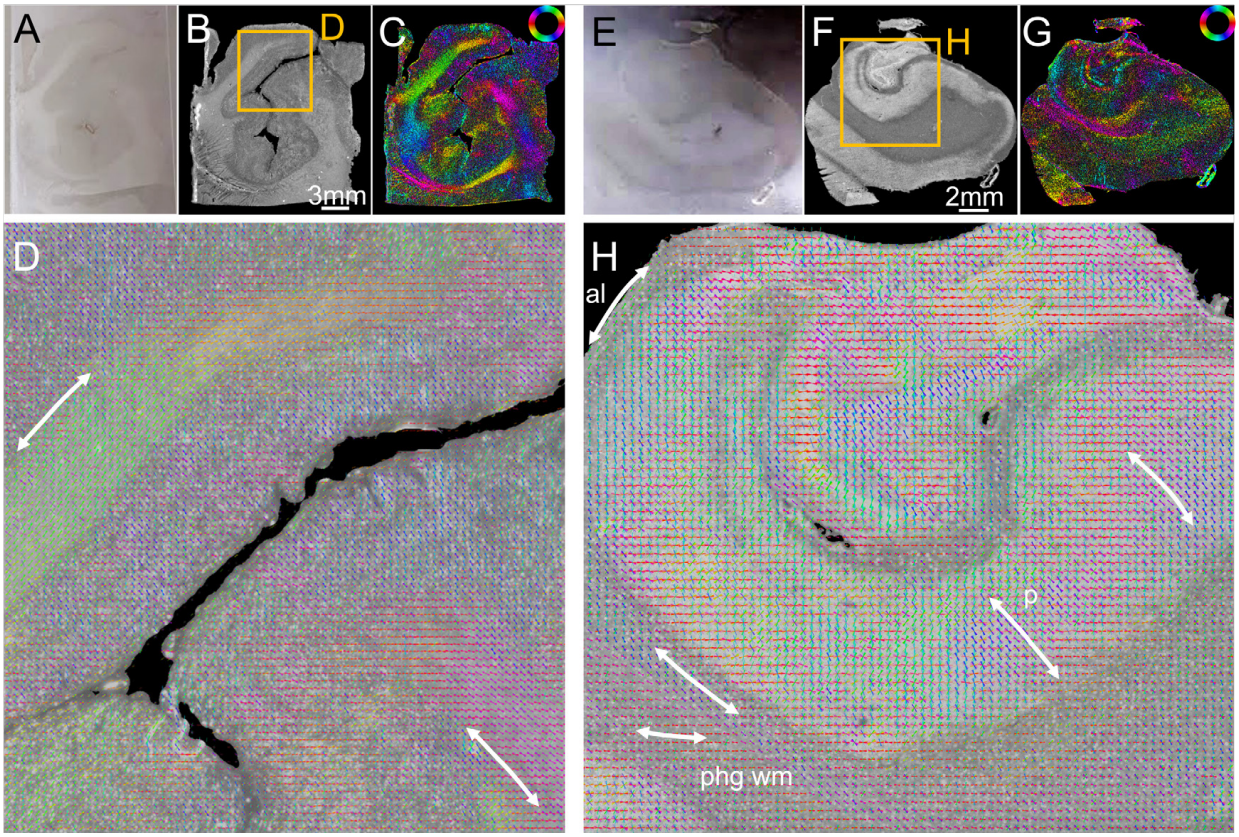

Supplementary Fig. 5 | ComSLI on uncoverslipped fresh-frozen brain tissue sections (). (**A**) Human visual cortex, photograph of the frozen section. (**B**) ComSLI average scattering map, 8μm/pixel. (**C**) Corresponding fiber orientation map showing the fiber orientations for each pixel in different colors according to the color wheel at the top right. (**D**) Zoomed-in fiber orientation vector map (orange box in (B)), including part of two white matter tracts (arrows) with distinct fiber orientations. Vectors of 15x15 pixels are overlaid. (**E**) Human hippocampal body, photograph of the frozen section. (**F**) ComSLI average scattering map, 8μm/pixel, including the Cornu Ammonis subfields (bright) and surrounding white matter (dark). (**G**) Corresponding fiber orientation map. (**H**) Zoomed-in fiber orientation vector map (orange box in (F)), depicting the convoluted tracts of the hippocampus, including the alveus (al), the parahippocampal gyrus white matter (phg gm), and the perforant pathway (p). Vectors of 15x15 pixels are overlaid.

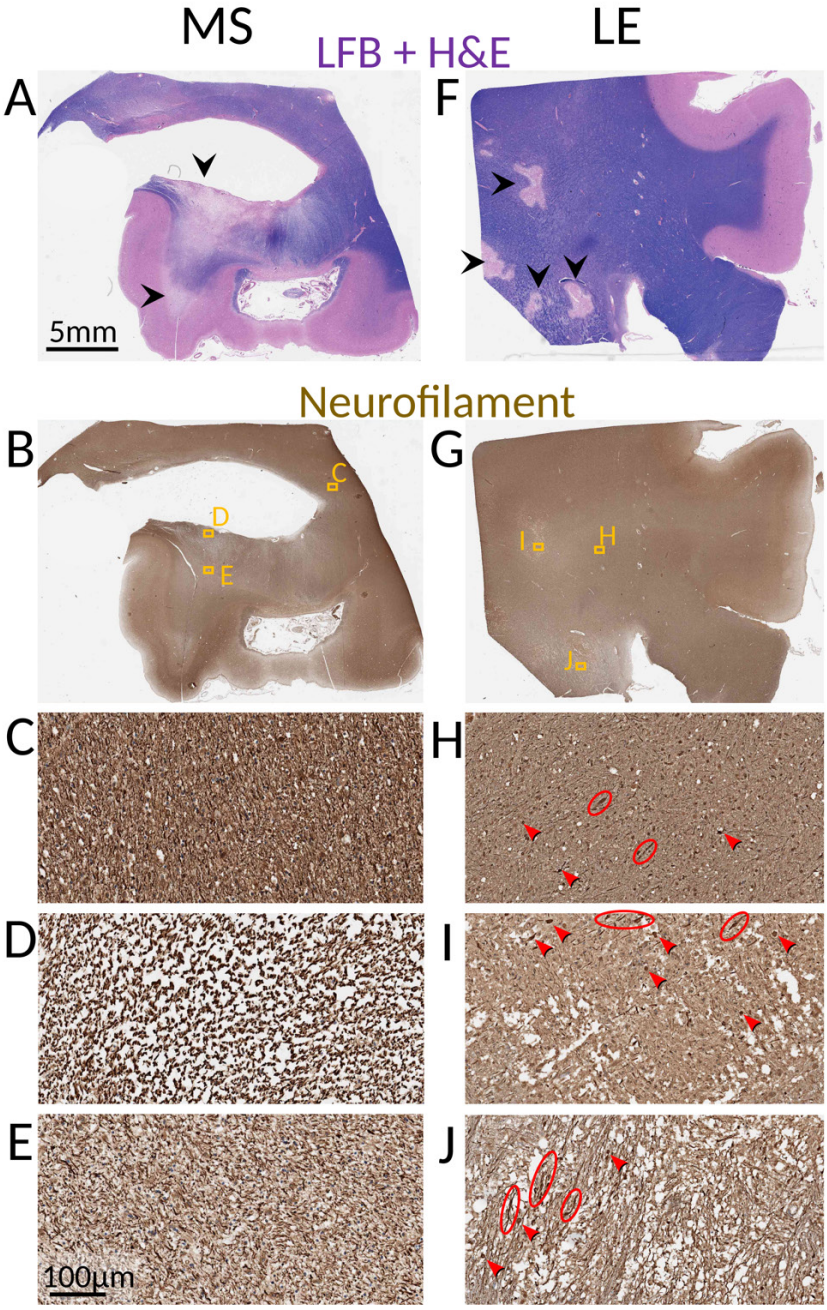

Supplementary Fig. 6 | Multiple sclerosis (MS) and leukoencephalopathy (LE) brain samples from main Fig. 3 (LFB+H&E and neurofilament-stained). (**A**) Multiple sclerosis brain section with Luxol-fast-blue (LFB) and hematoxylin & eosin (H&E) stain; LFB stains myelin blue, showing the demyelinating gradient, with minimal myelin left near the ventricle and the cortex (arrowheads). (**B**) Consecutive neurofilament-stained section, with orange boxes zoomed-in in C-E. (**C**) Normal-appearing white matter with neurofilament stain, with high density of neurofilament stain and healthy cell nuclei. (**D**) High myelin loss region, with oblique axons and tissue separation leading to low ComSLI signal in main Fig. 3B. (**E**) Region of lower myelin loss, with preserved axons, lower stain and nuclei density, leading to a bit lower scattering signal only in main Fig. 3B. (**F**) Leukoencephalopathy brain section LFB+H&E stained, with distinct fully demyelinated lesions (black arrowheads). (**G**) Consecutive neurofilament-stained section, with orange boxes zoomed-in in H-J. Examples of axonal spheroids and thickened dystrophic axons are indicated by red arrowheads and ellipsoids, respectively. (**H**) Relatively normal-appearing white matter with neurofilament stain, with high density of neurofilament stain and healthy cell nuclei, with only occasional axonal spheroids and dystrophic axons. (**I, J**) More involved areas of partial spongiosis and disrupted axons, with region-wise sparser stain and lower nuclei density.

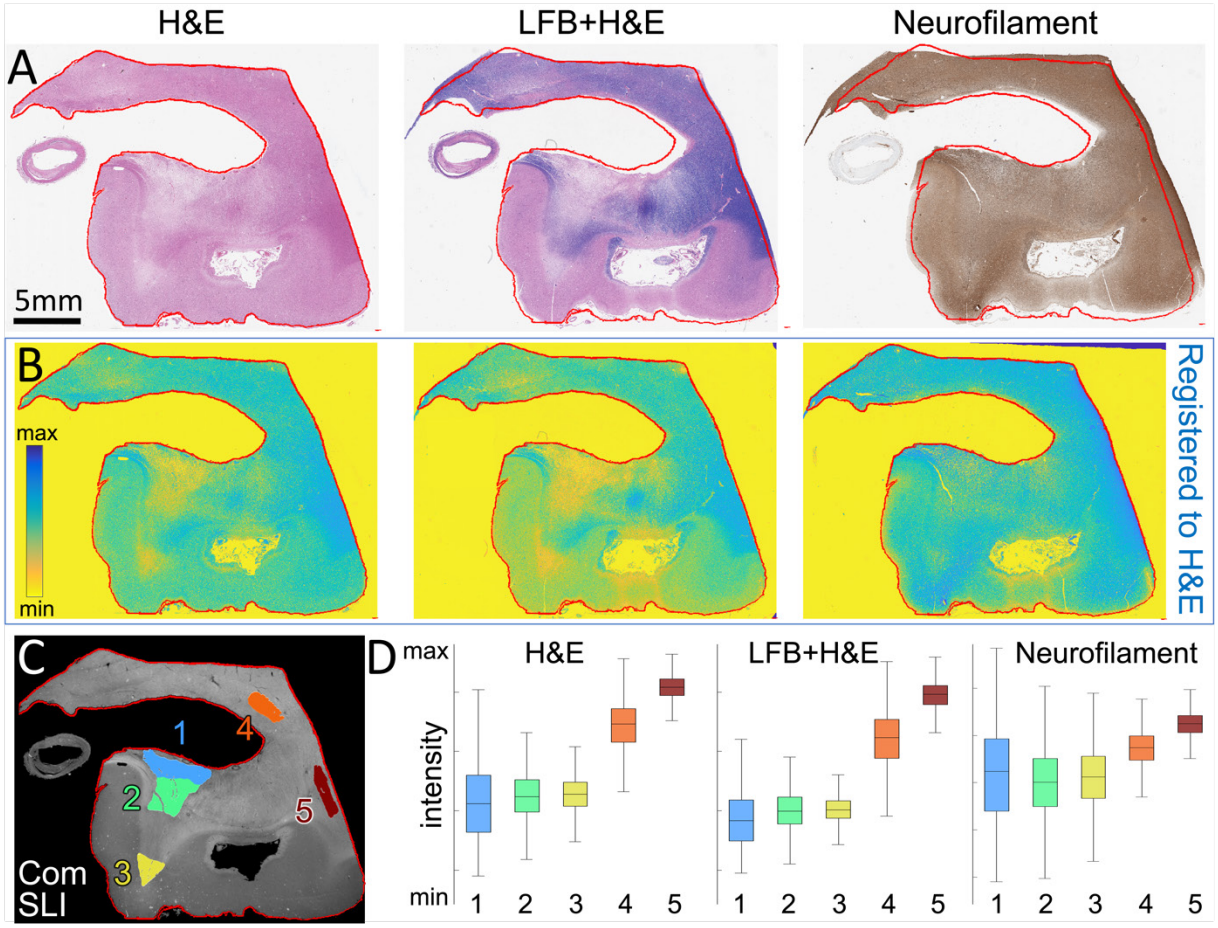

Supplementary Fig. 7 | Consecutive histology staining of human brain section with multiple sclerosis. **(A)** Brightfield images of the hematoxylin and eosin (H&E), luxol fast blue (LFB), and neurofilament-stained consecutive sections, with a red contour indicating the outline of the H&E section which is slightly different from the LFB and neurofilament section contours. (**B**) Color intensity maps of the three sections after being registered to the H&E section, with the contour accurately matching each section contour. The registration enables quantification of the stain intensities in the lesion and normal white matter areas as annotated in main Fig. 3A. (**C**) Average scattering signal from a ComSLI measurement of the H&E stained brain section. Colored regions mark lesion areas 1-3 and normal white matter areas 4-5, the same areas indicated in main text Fig. 3. (**D**) Box plots showing the average stain intensity signal in the different areas. The signal quantification shows a clear differentiation of demyelinated areas (1-3) compared to normal myelinated areas (4-5) by H&E and LFB+H&E, with very similar values, and a less clear differentiation using neurofilament stain intensity.

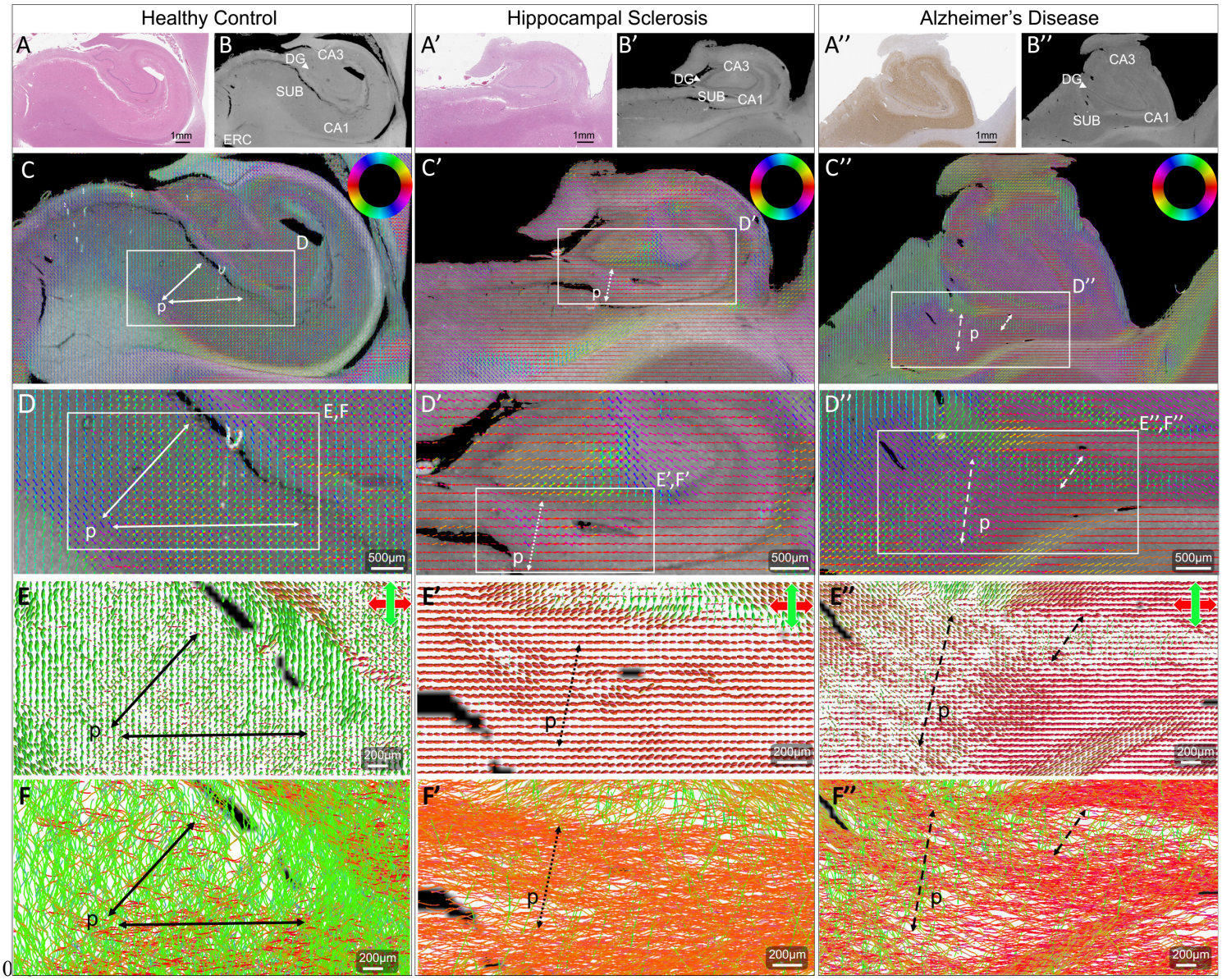

Supplementary Fig. 8 | Degenerative changes in human hippocampal tracts visualized with ComSLI. Left: healthy hippocampus (H&E-stained FFPE section). Middle: hippocampus with epileptic hippocampal sclerosis (H&E-stained FFPE section). Right: hippocampus with Alzheimer's disease (tau-stained FFPE section). (**A**) Bright-field microscopy images, 0.5µm/pixel. (**B**) ComSLI average scattering maps, 7µm/pixel, with hippocampal subfields identified (SUB: subiculum, DG: dentate gyrus, CA1/3: cornu ammonis 1/3, ERC: entorhinal cortex). Note that tissue tears are present in the subiculum in both control and sclerotic specimens. (**C**) Fiber orientations, overlaid for sets of 15x15 pixels, with orientations encoded by the orientation of the lines and their color, corresponding to the color wheel in the top right. Perforant pathway (p) directions are indicated by arrows. (**D**) Zoomed-in fiber orientation vector maps (white boxes in C), including the perforant pathway crossing the subiculum and/or CA1. Vectors of 15x15 pixels are overlaid. (**E**) Orientation distribution functions (ODFs) representing fiber orientations at 50µm resolution, with perforant tract directions highlighted. (**F**) Tractograms derived from the ODFs. The control perforant pathway shows strong connections (black arrows), whereas the perforant pathway tracts in the sclerotic hippocampus (F') are very scarce, and significantly reduced in the Alzheimer's Disease hippocampus (F").

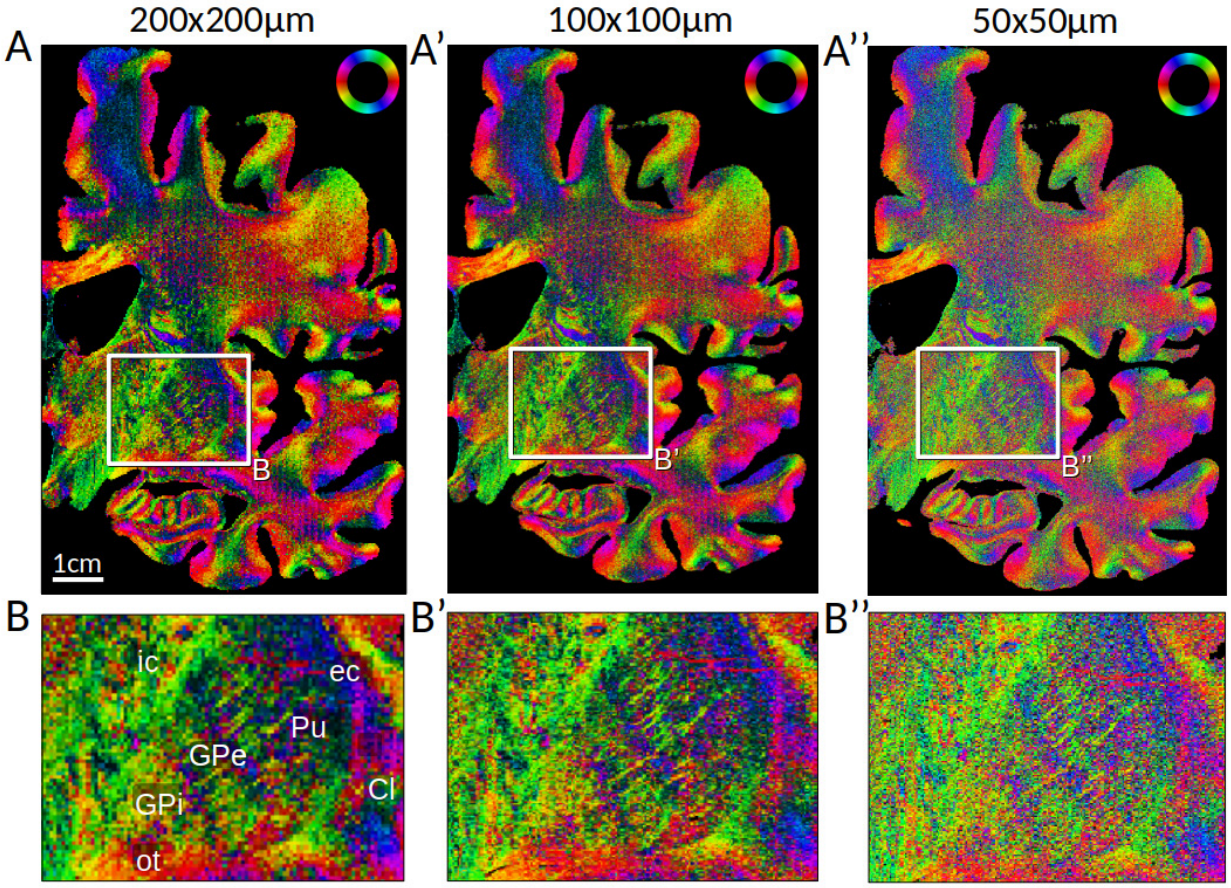

Supplementary Fig. 9 | Nissl-ST fiber orientations computed for different kernel sizes. (**A**) Fiber orientations of the Cresyl-violet stained brain section no. 3301 from main Fig. 4A computed from the brightfield microscopy image (1µm/pixel) with the provided code for Nissl-ST[25], using 15µm blur radius and a kernel size of 200x200µm, 100x100µm, and 50x50µm. (**B**) Zoom-in of the rectangular areas marked in (A), with anatomical regions labeled as in main Fig. 4B.

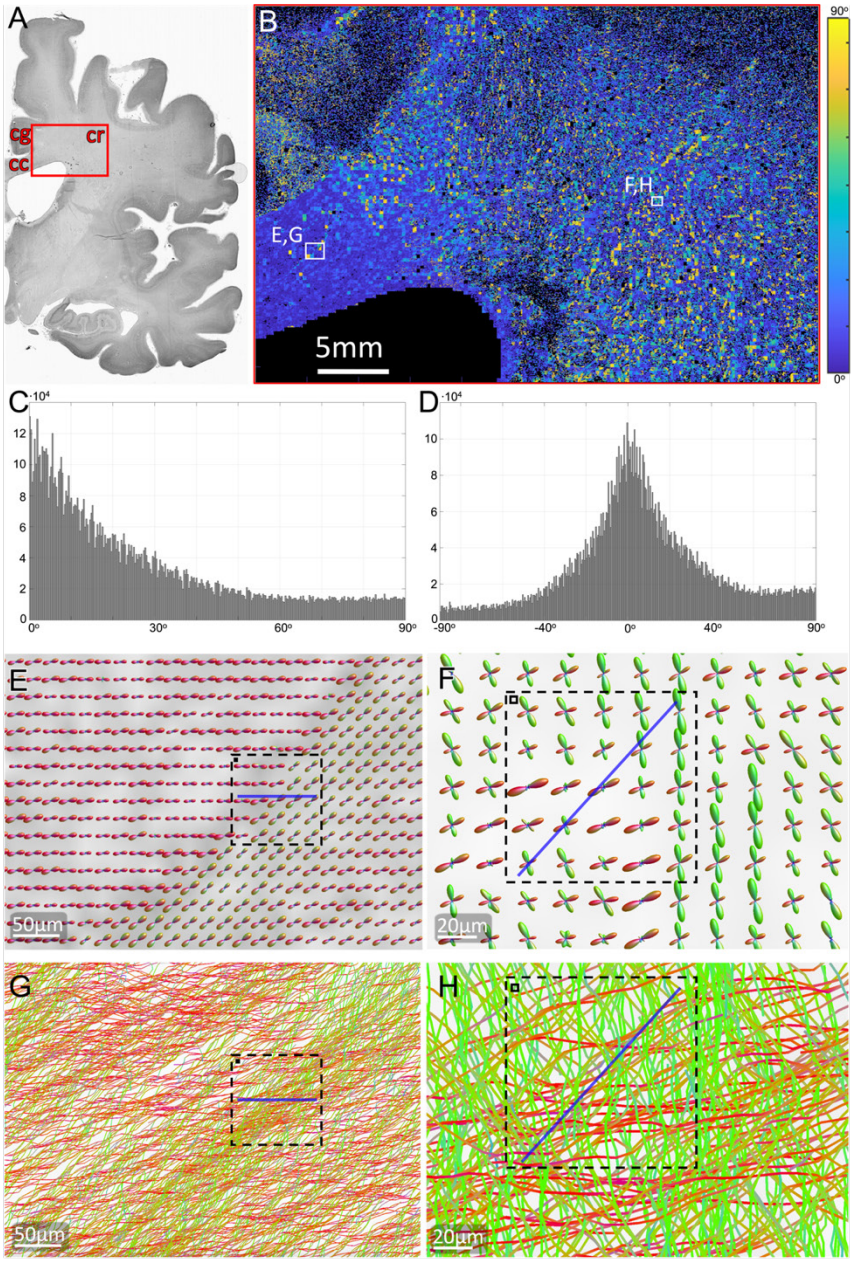

Supplementary Fig. 10 | Difference between ComSLI and Nissl-ST fiber orientations. (**A**) Histology image of the Cresyl-violet stained brain section no. 3301 from main Fig. 4A, with the analyzed area marked by a red rectangle, containing part of the corpus callosum (cc), cingulum (cg), and corona radiata (cr). (**B**) Absolute angle difference map between ComSLI and Nissl-ST fiber orientations. The map shows high agreement in the corpus callosum area, with only a few Nissl-ST pixels misaligned, but a wide range of angle differences in the corona radiata, as also exemplified in main Fig. 4D,D', where Nissl-ST misidentifies the single fiber orientation angles due to the existence of abundant crossing fibers. (**C**) Histogram of absolute angle differences, showing a skewed distribution towards 0° but also significant populations of orientation differences across the angular spectrum. (**D**) Histogram of signed angle difference (ComSLI - Nissl-ST), showing a similar pattern as C, centered around 0°. (**E-F**) ComSLI-derived orientation distribution functions (ODFs) of the corpus callosum and corona radiata areas indicated by white boxes in B, computed for kernels of 7x7 pixels (~20µm). The size of a Nissl-ST pixel (100µm) is indicated by a dashed square, whereas the size of a ComSLI pixel is indicated by a solid square at the top left corner of the dashed square. The derived Nissl-ST orientation for the particular pixel is shown with a blue line. (**G-H**) Tractograms of the same areas as in (E-F) computed from the ComSLI-derived ODF map, with fiber diameters set to approximately 1µm. Nissl-ST and ComSLI pixel sizes are indicated by dashed and solid squares as in (E-F), and Nissl-ST single pixel orientations are shown as blue lines.

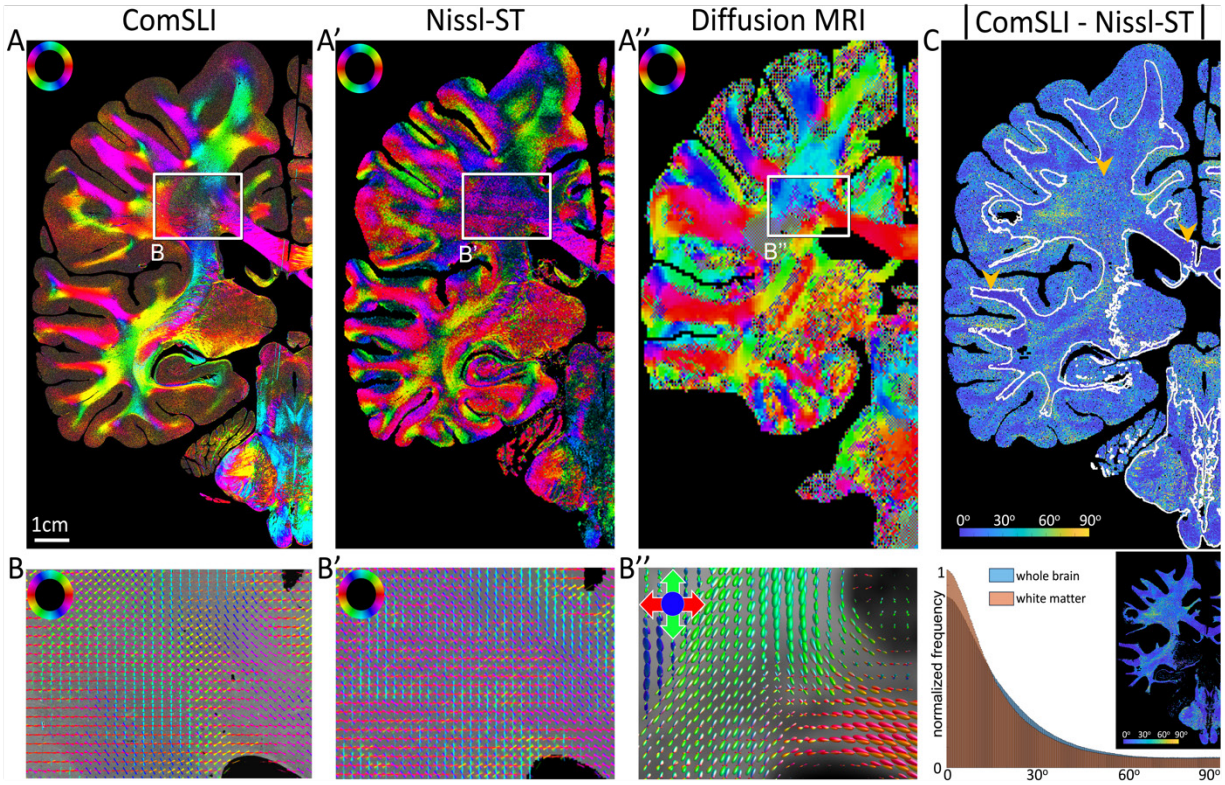

Supplementary Fig. 11 | Comparison of ComSLI, Nissl-ST, and dMRI fiber orientations for a silver-stained human brain section. ComSLI and Nissl-ST were performed on the same brain section (second *BigBrain* dataset, section no. 3452, FFPE, silver-stained, cf. main Fig. 1) – the ComSLI measurement with 9µm pixel size, and Nissl-ST on the brightfield microscopy image with 1µm pixel size and 100µm kernel size. Diffusion MRI was performed *in-vivo* on a healthy volunteer with 0.76mm isotropic voxel size, and the orientation distribution functions were evaluated at a plane similar to the evaluated brain section (see Methods). (**A**) Color-coded fiber orientations depicted for each image pixel. The orientations were computed with *SLIX*[34] for ComSLI and dMRI, and with the provided code for Nissl-ST[25], using 15µm blur radius and 100x100µm kernel. (**B**) Enlarged views for the rectangular area marked in (A), featuring crossing fibers in the corona radiata. ComSLI fiber orientations were visualized as colored lines and overlaid on 200x200 pixels for better visualization and comparison; Nissl-ST orientations were overlaid on 5x5 pixels; dMRI orientation distribution functions (ODFs) were visualized with *MRtrix3*'s *mrview*[35]. (**C**) Absolute difference between fiber orientations from ComSLI and Nissl-ST. The top image shows the difference map for the whole brain section (hemisphere), with arrows showing example white matter areas of mostly unidirectional fibers (left: superior temporal lobe; right: corpus callosum) where agreement is high, and crossing fibers (middle: corona radiata) where agreement is lower. The bottom histogram shows the distribution of the difference values for the whole brain section (red) as well as for white matter regions (blue) as indicated by the white outlines in the top image.

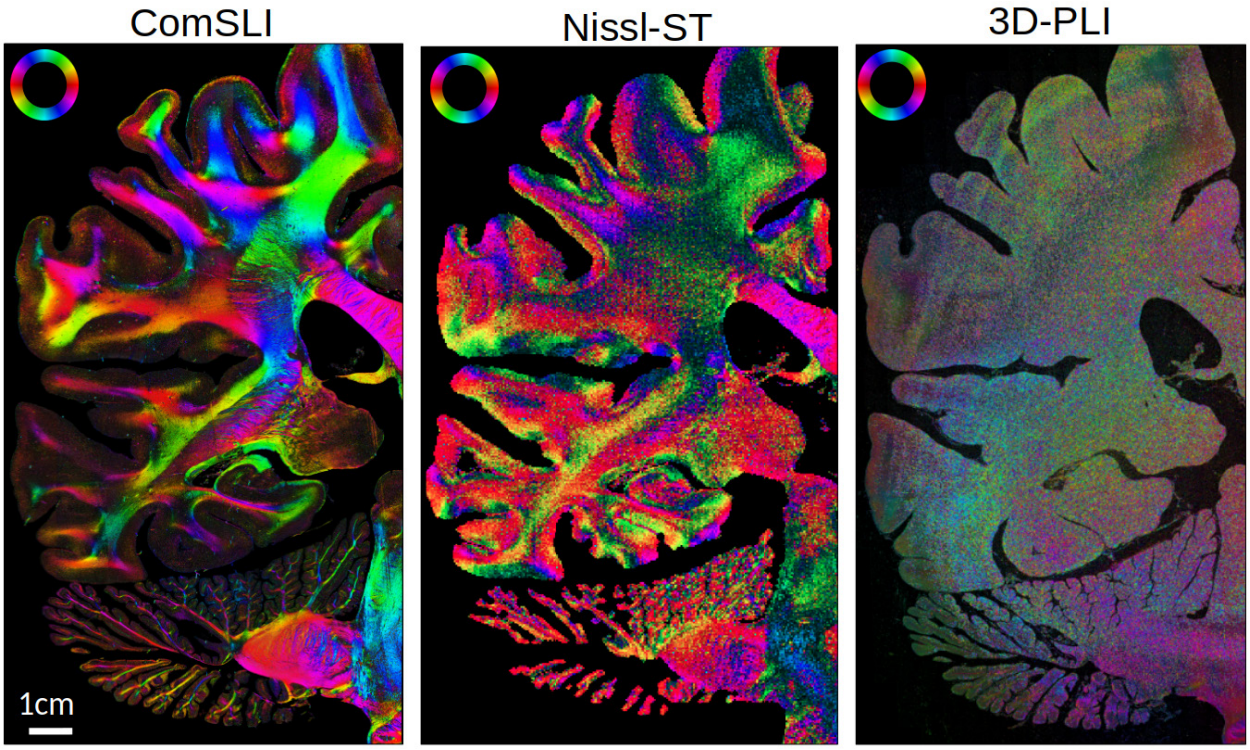

Supplementary Fig. 12 | 3D-PLI fiber orientation map of an FFPE brain section in comparison to those obtained by ComSLI and Nissl-ST. One hemisphere of a Cresyl-violet stained, human coronal brain section (no. 2520) was measured with 3D-PLI (1.85µm/pixel) and ComSLI (3µm/pixel), and the fiber orientations were computed for comparison. Due to brain preparation, the organization of myelin was destroyed and led to the loss of birefringence, going along with an impairment of fiber contrast in 3D-PLI measurements. The Nissl-ST fiber orientations were computed from the brightfield microscopy image (1µm/pixel) with 15µm blur radius and 100x100µm kernel size.

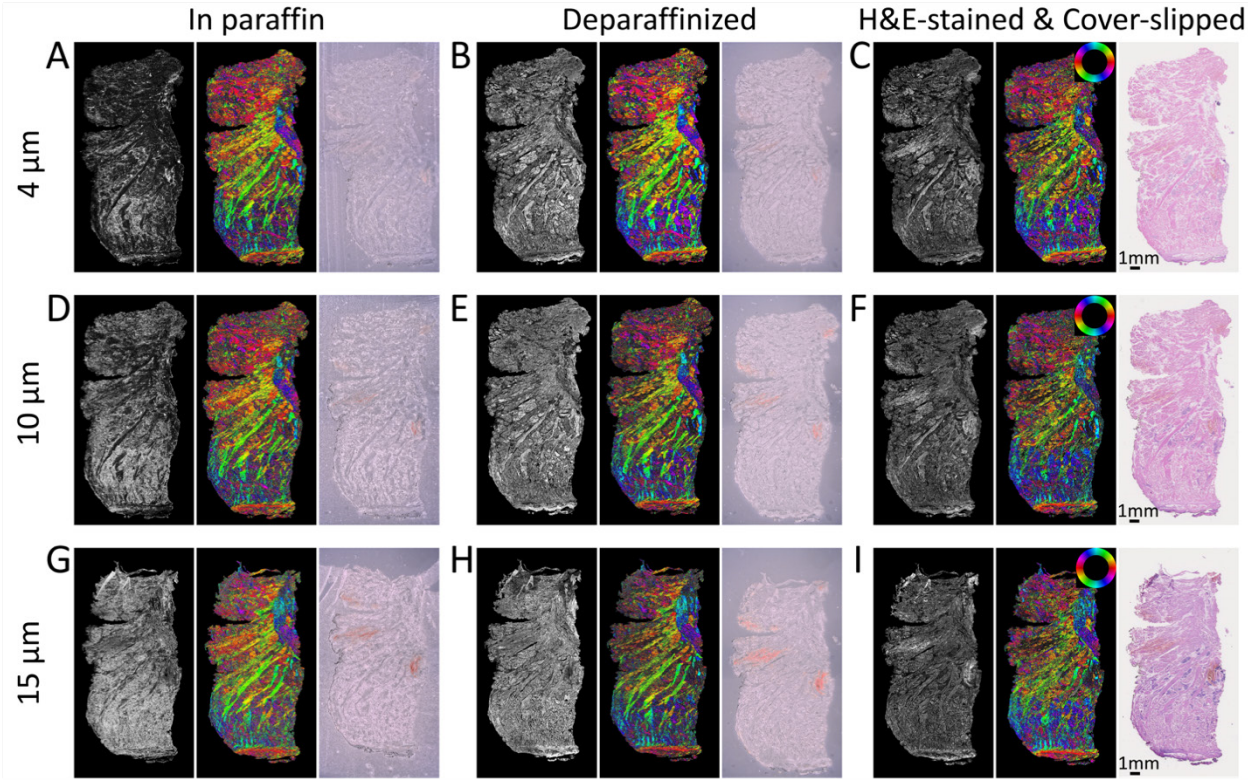

Supplementary Fig. 13 | Human tongue sections of 4µm, 10µm, and 15µm thickness measured with ComSLI at different steps of sample preparation. Each row corresponds to three different sample preparation steps of a single section of the indicated thickness. The left and middle images of each panel show the average scattering signal and the color-coded fiber orientations from ComSLI respectively (3µm/pixel), the right images show the corresponding brightfield microscopy images (0.46µm/pixel for H&E-stained sections, 10µm/pixel for the other sections). Panels in the left column (A,D,G) show the sections still in paraffin, unstained and without coverslip. Panels in the middle column (B,E,H) show the same sections after deparaffinization. Panels in the right column (C,F,I) show these sections after staining with hematoxylin and eosin (H&E) and cover-slipping.